Geophysical Journal International

Geophys. J. Int. (2013) **193,** 263–286 doi: 10.1093/gji/ggs083

Seismicity patterns along the Ecuadorian subduction zone: new constraints from earthquake location in a 3-D *a priori* velocity model

Yvonne Font,[1] Monica Segovia,[2] Sandro Vaca[2] and Thomas Theunissen[3]

[1] *Université de Nice Sophia-Antipolis, Institut de Recherche pour le Développement* (UR 082)*, Observatoire de la Côte d'Azur, Géoazur,* 250 *av Einstein* 06560 *Valbonne, France. E-mail: font@geoazur.unice.fr*
[2] *Instituto Geofisico, Escuela Politecnica Nacional, Quito, Ecuador*
[3] *Geosciences Montpellier, UMR* 5243*, CNRS, University of Montpellier* 2*, France*

Accepted 2012 November 22. Received 2012 July 6; in original form 2011 June 20

SUMMARY

To improve earthquake location, we create a 3-D *a priori P*-wave velocity model (3-DVM) that approximates the large velocity variations of the Ecuadorian subduction system. The 3-DVM is constructed from the integration of geophysical and geological data that depend on the structural geometry and velocity properties of the crust and the upper mantle. In addition, specific station selection is carried out to compensate for the high station density on the Andean Chain. 3-D synthetic experiments are then designed to evaluate the network capacity to recover the event position using only *P* arrivals and the MAXI technique. Three synthetic earthquake location experiments are proposed: (1) noise-free and (2) noisy arrivals used in the 3-DVM, and (3) noise-free arrivals used in a 1-DVM. Synthetic results indicate that, under the best conditions (exact arrival data set and 3-DVM), the spatiotemporal configuration of the Ecuadorian network can accurately locate 70 per cent of events in the frontal part of the subduction zone (average azimuthal gap is $289^\circ \pm 44^\circ$). Noisy *P* arrivals (up to $\pm$ 0.3 s) can accurately located 50 per cent of earthquakes. Processing earthquake location within a 1-DVM almost never allows accurate hypocentre position for offshore earthquakes (15 per cent), which highlights the role of using a 3-DVM in subduction zone. For the application to real data, the seismicity distribution from the 3-D-MAXI catalogue is also compared to the determinations obtained in a 1-D-layered VM. In addition to good-quality location uncertainties, the clustering and the depth distribution confirm the 3-D-MAXI catalogue reliability. The pattern of the seismicity distribution (a 13 yr record during the inter-seismic period of the seismic cycle) is compared to the pattern of rupture zone and asperity of the $M_w = 7.9$ 1942 and the $M_w = 7.7$ 1958 events (the $M_w = 8.8$ 1906 asperity patch is not defined). We observe that the nucleation of 1942, 1958 and 1906 events coincides with areas of positive Simple Bouguer anomalies and areas where marine terraces are still preserved on the coastal morphology. From north to south: (1) the 1958 rupture zone is almost aseismic and is attributed to a zone of high coupling; (2) south of the Galera alignment (perpendicular to the trench), the 1942 rupture zone presents moderate seismicity, deeper on the seismogenic interplate zone, and abutting on the Jama cluster (to the south). This cluster is facing the Cabo Pasado cap and positive Bouguer anomalies on the overriding margin. We suspect that this cluster reflects a zone of local asperity (partial coupling). South of the Jama cluster, the spherical aseismic zone in the Bahia area is interpreted as having a low seismic coupling (steady creep motion or slow slip events). We suspect that the site that generated the three $M > 7$ events (1896, 1956 and 1998) correspond to a small patch of strong coupling. To the south, in the Manta-Puerto Lopez zone, the seismicity is mainly organized in earthquake swarms (1998, 2002, 2005). Although slow slip events have been observed in the area (Vallée *et al.* submitted), we infer from the coastline shape, the marine terraces and the high positive Bouguer anomalies that the seismicity here might reveal a significant amount of seismic coupling.

Key words: Seismic cycle; Seismicity and tectonics; Computational seismology; Subduction zone processes; South America.

1 INTRODUCTION

Interplate seismogenic zones of subduction systems generate the most destructive earthquakes worldwide, as these faults are superficial (generally shallower than 60 km depth) and extend laterally along coastlines (Pacheco *et al.* 1993; Tichelaar & Ruff 1993; Heuret *et al.* 2011). However, the precise seismicity distribution and its temporal modification, particularly for small magnitude events, are often poorly assessed. Our comprehension of the interplate seismogenic zone behaviour is thus restricted in time, especially during the later part of the seismic cycle when seismicity is supposed to contribute to stress build up and concentrates around the periphery of the (future) rupture zone (Mogi 1979; Scholz 2002; Bollinger *et al.* 2004). The absolute position of earthquakes also contributes to the assessment of the seismic hazard because accurate event location is needed to determine magnitude and focal mechanism, as well as to highlight active fault geometry or seismic gaps. Improving absolute earthquake location from permanent seismic network monitoring is therefore crucial to better understand the seismic behaviour along subduction systems before a main shock.

In most subduction zones, limitations in assessing absolute earthquake location are specifically because of (1) scarce seismic monitoring near coastal areas and the lack of permanent marine networks and (2) the fact that the three-dimensional (3-D) aspect of the heterogeneous lithospheres is generally not considered. In most cases, earthquakes occurring on the interplate seismogenic zones are located offshore while seismic stations are deployed onland. Consequently, the network configuration causes azimuthal gaps often larger than 180° and large source-to-station distances (>50 km), which are not suitable for regional tomographic inversion or earthquake location (Bondar *et al.* 2004). This restricts our knowledge on 3-D structures and seismic velocity properties. Subsequently, 1-D velocity models are generally used despite the strong lateral seismic velocity variations found in subduction zones. When computed in 1-D media, predicted seismic ray traveltimes have large errors and generate significant mislocation in hypocentre determination (Lomax *et al.* 2001; Flanagan *et al.* 2007). Improving earthquake location in subduction zones, where deploying permanent network with efficient azimuthal coverage is difficult, requires improving traveltime estimates, which in turn essentially relies on the ability of the 3-D velocity model to represent structural intricacies such as: surface topography variations (from the oceanic trench to the volcanic arc), the compositional difference between an oceanic subducting plate and a continental overriding plates, lateral seismic velocity variations produced by local tectonic structures (such as subducting ridges, forearc sedimentary basin, magmatic chambers, backarc basin), crustal thickness and Moho discontinuity or mantle hydration.

A significant step in earthquake location consists in the establishment of *a priori* 3-D velocity model (3-DVM) to compensate the lack of precise tomography model. *A priori* velocity models are constructed in part or totally by integrating information on structures and velocities that results from independent investigations (e.g. reflection or wide-angle seismics, gravity, surface geology; Nataf & Ricard 1996; Ricard *et al.* 1996; Bhattacharyya *et al.* 2000; Pasyanos *et al.* 2001; Johnson & Vincent 2002; Font *et al.* 2003; Husen *et al.* 2003; Rhodes 2004; Flanagan *et al.* 2007; Font & Lallemand 2009). This type of models improves traveltime estimates and earthquake location accuracy as evidenced by the error reduction relative to reference events such as nuclear bombs for teleseismic hypocentre determinations or explosions and seismicity on well-known tectonic features for local studies.

In this paper, we propose a 3-D approach to improve earthquake location in subduction zones. The application's objective is to better resolve the seismicity distribution on or at the vicinity of the Ecuadorian interplate seismogenic zone. In this area, no precise tomography covering the whole active margin has been published, mainly because of the network configuration (Prevot *et al.* 1996). We thus construct and present the first *a priori* 3-D *P*-wave velocity model established from the integration of geophysical and geological investigations carried out on the Ecuadorian margin. The velocity model is available upon request to the first author. Hypocentre determination uses events recorded locally during the interseismic period, between 1994 and 2007, on the permanent RENSIG seismological network (*Red Nacional de Sismógrafos del Instituto Geofisco, Escuela Politecnica Nacional,* Quito). One of the main difficulties hinges upon the network configuration (essentially short-period and vertical component) that was initially installed to monitor volcanic hazards and is essentially deployed along the linear Andean Chain at about 200–300 km from the trench. The subsequent station density disequilibrium requires a specific data selection to enhance the effect of the few coastal stations on earthquake location (relative to the Andean stations).

We perform hypocentre determination using an improved version of the maximum intersection technique (MAXI; Font *et al.* 2004; Theunissen *et al.* 2012) as its search process is reduced to the direct search of the three unknowns (longitude, latitude and depth). The origin time of the earthquake is then solved from the solution position. Designing a *P*-velocity model alone is a choice motivated by the lack of knowledge about the 3-D *S*-velocity properties and the network characteristics (vertical component sensors). Before the application to real data, we design a 3-D synthetic experiment (that we called a resolution test) to evaluate the network capacity to recover true-event positions using only *P* arrivals. Applying the application to real data, we evaluate the effect of the 3-DVM by comparing the earthquake location to the results obtained, using the same arrival-time data set and technique, within a 1-D velocity model and to the initial solutions from RENSIG. Earthquake location results, from location uncertainties, confidence factors and geodynamic adequacy, attest to the efficiency of the *a priori* 3-D velocity model presented in this study to improve hypocentre location in the Ecuadorian subduction zone. To conclude, we discuss the new event catalogue compared to the rupture zones of the four historical earthquakes that occurred in the area.

2 *A PRIORI* 3-D *P*-WAVE VELOCITY MODEL IN ECUADOR

This study consists in the construction of a 3-D georealistic *P*-velocity model (3-DVM) to compensate for the lack of a precise tomography model. We create the *a priori* model by integrating published information on structures and velocities that we could gather on Ecuador (or comparable subduction zones). The resulting model is totally independent of tomographic inversions and recovers, as well as possible, the first-order lithospheric variations in terms of geometry and velocity. The model extends from northern Peru (6.5°S) to southern Colombia (3°S), between 277°E and 283°E and reaches 300 km depth. The parametrization of the velocity model is discussed at the end of this chapter. The following section presents the information we used to construct the velocity model.

2.1 Geodynamic, structural and velocity data

Subduction occurs beneath northern South America since at least Early Jurassic time (Aspden *et al.* 1987; Jaillard *et al.* 1990; Kerr & Tarney 2005). Many works have been conducted onland and offshore which allow reconstructing the geodynamic evolution of the region and highlight the complexity and 3-D structure of the Ecuadorian subduction system. For the purpose of a 3-DVM construction, we summarize those works, distinguishing four main structural units over the southern Colombia—northern Peru region. Each of them has its own geometry and seismic velocity properties that one needs to consider to improve wave propagation computations. The structural units are: The Nazca Plate and associated downgoing slab, and the overriding plate composed of three regions: (1) the continental Guyana Shield and sedimentary basin (east of the Andes), (2) the Andean Chain and inter-Andean valley (both a volcanic arc and geological suture) and (3) the North Andean Block composed of accreted oceanic plateaus and a thick sedimentary cover (Figs 1 and 2). Note that in the presentation of the model construction and structural units, we refer under the term "North Andean Block" to the part of the block that extends from the trench to the western Andes foothills. The real limit of the North Andean Block is still debated but we know it is located eastward, along the Andean Chain, and that it extends from the Puna Island to north of Venezuela.

The surface topography included in the 3-DVM is irregular and presents huge variations from about −4000 m near the trench to +6000 m at some active volcanoes (Michaud *et al.* 2006). The trench-to-coast distance (from 50 to 190 km) and trench geometry vary laterally along the subduction, increasing in obliquity from ∼10° in Central Ecuador, to ∼30° in southern Colombia (Trenkamp *et al.* 2002).

2.1.1 *The Nazca Plate*

The age of the Nazca Plate (subducting beneath the South America Plate) and its segmentation varies along the subduction zone, mainly

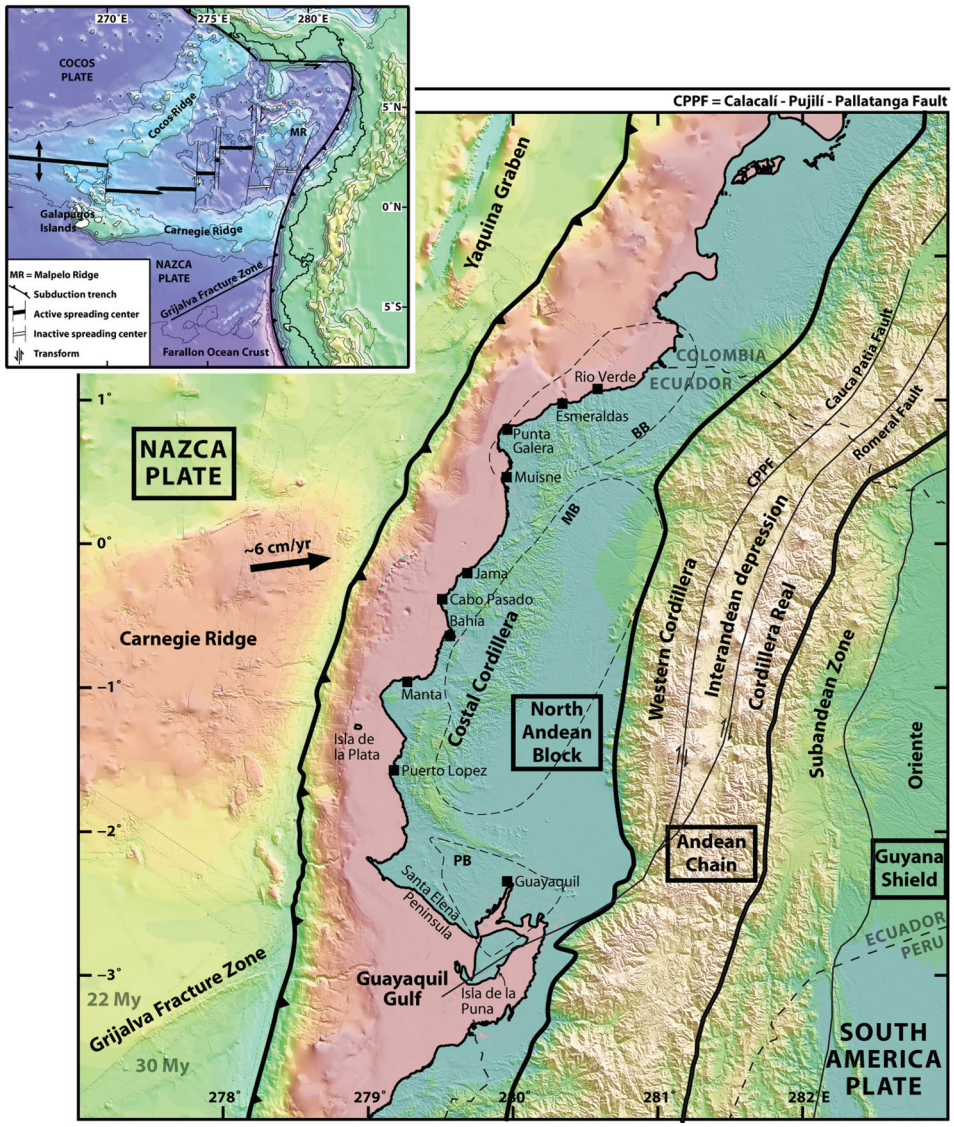

Figure 1. Geodynamical framework of the Ecuadorian subduction zone. Simplified faults traces modified from Vallejo *et al.* (2009): CF = Cosanga Fault; CPPF: Calacalí – Pujilí – Pallatanga Fault. Bathymetry/topography map from Michaud *et al.* (2006). Limits of the main sedimentary basins from Deniaud (2000): BB = Borbon Basin; MB = Manabi Basin; PB = Progreso Basin.

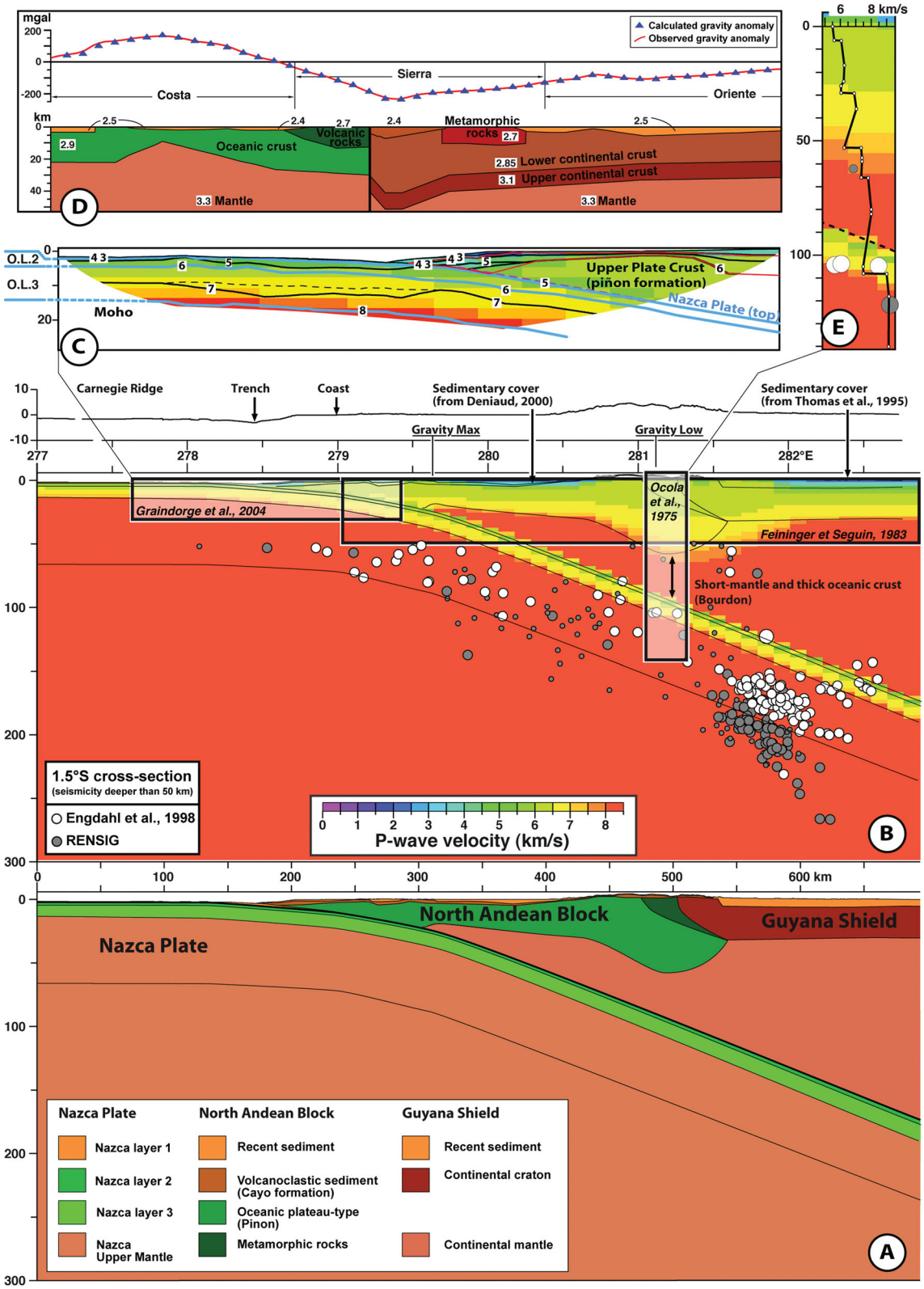

Figure 2. (a) Example of the lithospherical and upper mantle model of Ecuador along an E–W cross-section at 1.5°S established for the construction of the 3-DVM; thin lines define the principal limits of the structural units (sedimentary layer, crustal basement and upper mantle, for both tectonic plates—see colour code within the figure). (b) Cross-section within the velocity model and geophysical data existing at (or near) this latitude (active seismic refraction from Graindorge *et al.* (2004) and Ocola *et al.* (1975); crustal model from Simple Bouguer gravity field of Feininger & Seguin (1983); seismicity distribution from Engdahl *et al.* (1998, in white) and RENSIG (in grey). Thin lines define the same principal limits of the structure shown in (a); (c) Active seismic refraction model from Graindorge *et al.* (2004). (d) Crustal profile determined from Bouguer anomalies (Feininger & Seguin 1983). (e) 1-D velocity model along the Andean Chain resulting from the Nariño active seismic experiment (from southern Colombia to central Ecuador, from Ocola *et al.* (1975)).

because of the Farallon Plate splitting along a preexistent NNE fracture zone during Oligocene time (~ 30–25 Ma; Hey 1977). The crust is about 30 Ma south of the Grijalva Fracture Zone, 22 Ma north of it, and decreases northwards to about 10 Ma at the southern limit of the Yaquina Graben (Fig. 1; Lonsdale 1978, 2005; Lonsdale & Klitgord 1978). The rupture of the Farallon oceanic plate evolved into the E–W trending Cocos-Nazca Spreading Center. Around 23–20 Ma, the interaction between the Galapagos Hot Spot and the spreading centre results in the formation of the Cocos (and Malpelo) Ridge north of the spreading centre and the Carnegie Ridge south of it (Sallares & Charvis 2003). Near the Ecuadorian Trench, the aseismic Carnegie Ridge is about 280 km wide and 2 km high with respect to the neighbouring abyssal plain.

The oceanic crust thickness varies laterally beneath the overriding margin as observed on wide-angle data, reaching up to 19 km beneath the Carnegie Ridge crest (Sallares & Charvis 2003) and 14 km on its southern flank (central Ecuador; Calahorrano 2001; Graindorge *et al.* 2004) and thinning down to 5 km off southern Colombia (Meissner *et al.* 1977; Garcia 2009). Near the trench, oceanic basement velocities vary from ~5 km s^{-1} (at the top of oceanic layer 2) to ~7.0 km s^{-1} at the base of oceanic layer 3 (Figs 2b and c). The Moho discontinuity is represented by a strong velocity gradient from ~7 to 7.8 km s^{-1} in less than 1 km of depth (averaged from (Graindorge *et al.* 2004; Agudelo *et al.* 2009).

The Ecuadorian margin is highly segmented and mainly erosional (e.g. Collot *et al.* 2002). Sedimentary variation of trench filling, downgoing subduction channel thickness, physical properties and/or patchiness on the interplate, accretionary prism, frontal forearc basins and also shallow interplate dip angle are given by Calahorrano *et al.* (2008), Collot *et al.* (2004, 2008), Marcaillou & Collot (2008), Sage *et al.* (2006), Witt *et al.* (2006). The shallowest part of the 3-DVM is constrained by these structural data.

Along-strike structural variations may be described along four segments.

(1) North of the Esmeraldas Canyon (*Manglares* segment after Marcaillou *et al.* 2006), the trench is locally disrupted and filled by ~3 km of turbidites. The accretionary prism is less than 5 km wide or absent (Collot *et al.* 2008). The narrow shelf (5–20 km) is affected by an 80 km wide and ~1 km deep reentrant (Collot *et al.* 2004; Marcaillou *et al.* 2006). Near the trench, the Nazca Plate dips about 7.5° eastward (at ~4.5 km depth) and is only slightly affected by normal faults (contrarily to the northern Colombian segment; Marcaillou *et al.* 2006). The downgoing subduction channel is about 2 km thick and is considerably reduced at 60 km from the trench (~15 km depth; Agudelo *et al.* 2009). The Nazca crust thickness is about constant (6.5 km) from the oceanic basin to 60 km east of trench (Agudelo *et al.* 2009).

(2) Between the Esmeraldas canyon and the northern extent of the Carnegie Ridge (1.5°N–0.5°N), the continental shelf widens to 50 km and shallows to less than 100 m (Collot *et al.* 2004). The well-marked trench deepens to ~3.7 km and contains up to 500 m sedimentary fill (Collot *et al.* 2002). The Nazca Plate lies at ~5 km depth beneath the trench fill. The dip angle is 3° along 35 km from the trench and increase to ~15° eastward.

(3) Along the Carnegie Ridge segment, the trench shallows to ~2.8 km and contains only a few turbidites (Lonsdale 1978; Collot *et al.* 2004). The interplate boundary is dipping 10° 15 km from the trench. A thin subduction channel locally thickens to form low-velocity 600-m-thick lenses of underthrusted fluid-rich sediment (Sage *et al.* 2006).

(4) Between the Carnegie Ridge and the Grijalva Fracture Zone, the trench is narrow (3–4 km wide), at 4 to 4.2 km depth and contains about 300 m of infill deposit (2–2.2 km s^{-1}; Calahorrano *et al.* 2008). The accretionary prism widens to 3 km. The subduction channel is thin (maximum of 0.6 km) and imaged to 25 km landward from the trench (~7.5 km deep). The Nazca Plate is locally dipping landward at 6°. Off the Gulf of Guyaquil, a 3–10 km wide and 1 km thick sedimentary prism fronts the margin (Calahorrano *et al.* 2008). Sediment accumulation is favored south of the Grijalva Fracture Zone because the trench is deepest. The trench is 10 to 15 km wide, about 4.8 km deep and filled by about 500 m of sediment. The subduction channel is visible from the trench (0.2 km thick) reaching a thickness of ~1 km before thinning to only 0.3 km at ~30 km of the trench landward (low velocity 2.8 km s^{-1} relative to the 3.5–3.8 km s^{-1} of the overlying upper-plate basement). The Nazca crust is at 4.5 km depth before trench.

At greater depth (between 40 and 300 km), as imaged by local seismicity, the downgoing slab dip-angle does not vary significantly, although it is slightly higher to the north and lower in northern Peru. A flat slab had been proposed beneath Ecuador based on scarce teleseismic records (Gutscher *et al.* 1999) but is controversial based on other local seismicity observations. Indeed, in northern Ecuador, at depths greater than 30 km, the slab dips about 25–30° down to 140 km depth (Pontoise & Monfret 2004; Manchuel *et al.* 2009; Manchuel *et al.* 2011), 25–35° down to 200 km in Central Ecuador (Prevot *et al.* 1996; Guillier *et al.* 2001) and reduces to about 25° in northern Peru (Tavera *et al.* 2006).

In the 3-DVM, the slab geometry is extrapolated from both local (RENSIG) and teleseismic catalogues [EHB catalogue from Engdahl *et al.* (1998); Fig. 2b]. In the northern part of the country, the 1-D deep seismic profile, resulting from the Nariño active seismic experiment (Ocola *et al.* 1975), is also taken into consideration (Fig. 2e). When not clearly constrained by seismicity, the slab depth beneath active volcanoes is forced to range between 80 and 120 km depth (Fig. 2b). Slab dip is considered constant down to 300 km depth. Seismic velocities beneath the oceanic Moho are taken from the iasp91 model (Kennett & Engdahl 1991).

2.1.2 Guyana shield and sedimentary cover

The Nazca Plate underthrusts the South America Plate. East of the Andes, the Amazon Basin (or *Oriente*) is a Mesozoic to Cenozoic, hydrocarbon-rich sedimentary foreland basin that includes a platform carbonate sequence, overlying the older cratonic Guyana basement, both intruded by large granitoid batholiths along the boundary with the Andes (Christophoul *et al.* 2002; Hughes & Pilatasig 2002; Cediel *et al.* 2003). The sedimentary thickness reaches 10 km (Thomas *et al.* 1995) and is characterized by a velocity gradient between ~2 to 5.5 km s^{-1}. From gravity modelling, the average continental crust thickness is estimated between 30 to 35 km (Fig. 2d; Feininger & Seguin 1983). Velocities increase from 5.8 km s^{-1} (at top of continental basement) to 6.8 km s^{-1} near the Moho discontinuity.

2.1.3 Andean chain and inter-Andean valley

West of the Amazon Basin, the Ecuadorian Andes, in broad approximation, consists of two parallel ranges, oriented NNE–SSW and reaching about 6 km of elevation: the Western Cordillera (to the west) and the Real Cordillera (to the east). The Real Cordillera consists mostly of sub-linear belts of Palaeozoic to Mesozoic metamorphic rocks, accreted to the palaeo-continental margin since

the Mesozoic (Aspden *et al.* 1992). They are covered by Cenozoic to modern volcanosedimentary units. The Western Cordillera consists of a volcanic arc that lies astride a basement composed of accreted oceanic plateau (same basement as the coastal area; Hughes & Pilatasig 2002). Both cordilleras are separated by the inter-Andean graben filled by Pliocene and Quaternary volcanosedimentary rocks (sedimentary velocity for about 5 km of thickness; Fig. 2d). Feininger & Seguin (1983) suggest that the basement underlying the inter-Andean graben consist of Real Cordillera rocks. The inter-Andean graben and active Calacali-Pujili Fault zone (at the eastern limit of the Western Cordillera) is considered as marking the suture zone between the continental basement to the east and the oceanic one to the west. Within the 3-DVM, seismic velocities are subsequently slightly lower in the Real Cordillera than in the Western Cordillera. The crustal depth and reflective Moho is not well constrained in this area. Active seismic, seismology and gravity modelling agree with a crust thickness reaching between 50 and 66 km depth (Ocola *et al.* 1975; Leeds 1977; Feininger & Seguin 1983; Prevot *et al.* 1996; Guillier *et al.* 2001) but no strong Moho discontinuity has been seen. In the 3-DVM, east and west and the Andean Chain, the Moho is represented, at near 30 km in depth, by a strong velocity gradient (from ∼7 to 8 km s^{-1} in less than 2 km thick layer). Beneath the Andean Chain, the Moho gradient is significantly smoothed and the velocities of 7 and 8 km s^{-1} are marked at 55 and 65 km depth, respectively.

2.1.4 North Andean block and forearc basins

West of the Andes, the Coastal Plain basement is characterized by allochthonous oceanic terranes accreted to the continental margin during Cretaceous to mid-Eocene times that are locally exposed in the Coastal Cordillera (Litherland & Aspden 1992; Kerr *et al.* 2002). Three thick sedimentary basins overlay the oceanic basement and cover a large part of the Coastal Plain (Daly 1989; Deniaud 2000). From north to south, they are Borbon, Manabi and Progreso basins. Sedimentary fill may reach up to 10 km. The seismic velocities within the forearc basins increase with the sedimentary thickness, reaching about 5 km s^{-1} for a thickness of about 8 km. Based on gravity modelling (Case *et al.* 1973; Feininger & Seguin 1983), the North Andean Block crustal thickness varies between 22 km (near the coast line) to 30 km (western flank of the Andes), locally thinning beneath the Coastal Cordillera. The crustal seismic velocity gradient increases from 4.8 to ∼7 km s^{-1}.

2.2 Constructing the velocity model and grid parametrization

To construct the 3-DVM, we integrate on a series of vertical E–W cross-sections (each 0.5°) the multiple and independent geological/geophysical observations described above to differentiate the structural units (sedimentary layers, crustal basement and upper mantle, for both tectonic plates) in terms of geometry as well as *P*-velocity (V_P) gradients. Structural geometry and V_P gradients are used to characterize the top and bottom of the envelopes that limit each unit in space. The final model is obtained by interpolating the seismic velocities to the whole region and by averaging seismic velocities in blocks of constant velocities (Fig. 3). The technical approach is similar to that used by Font *et al.* (2003).

The gridding of the velocity model is parametrized into a blocky schema, following the approach presented by Zhou (1994). Horizontally, the studied area covers 648 × 1092 km^2, with *x* and *y* axes following E–W and N–S directions, respectively. The SW corner is assigned to be the origin point, at 277°E and 6.5°S. The heterogeneous velocity structures are characterized by a set of non-overlapping, equal volume and constant V_P velocity blocks. Each block dimension is 12 × 12 × 3 km in the *x*, *y* and *z* directions, respectively. Therefore, structures thinner than 3 km (such as the subduction channel, for instance) are incorporated in the average velocity of the concerned blocks. The entire velocity model consists of 516 120 blocks. In accordance with the shortest ray path method (Moser *et al.* 1992), ray tracing nodes are placed only on facets, edges and vertices of blocks and each of them has a constant slowness ($1/V_P$). Because blocks are of constant velocity, that is straight ray path within each block, there is no need for nodes inside the blocks. The interval between two adjacent nodes is 3 km along the horizontal directions and 1 km vertically. Each block consists of 82 nodes and 15 745 384 nodes constitute the whole velocity model. This parametrization is propitious for the dimension of our velocity model but it shall be adapted accordingly to the size of the region under study (Theunissen *et al.* 2012).

In summary, the 3-DVM constructed here integrates the data known on the heterogeneous crust and mantle velocities, mimicking the topography variations, the sea water and air columns, the sedimentary layers and crustal thicknesses, the crustal lithologies and the slab dip angle. The model includes the effect on near-surface seismic-wave velocities produced by some local tectonic structures such as the Carnegie Ridge or the Inter-Andean Valley. The 3-DVM aspires to represent, at least in broad lines, realistic velocity variations to better control traveltime estimates in a region where local tomography does not exist.

3 SEISMOLOGICAL DATA

Since 1990, the RENSIG is recording the seismic activity in Ecuador (Segovia & Alvarado 2009). This study uses the arrival times manually picked by the staff of the Institute of Geophysics of the events recorded between 1994 and 2007. During this period, the RENSIG documented about 44,000 seismic events. The network is telemetered and essentially composed of vertical component, short-period stations. Accurate subduction earthquake location is complicated because of the seismological network configuration, which has been for the last 15 yr essentially distributed over the Andean Chain to monitor volcanic hazard. The distribution of the seismic stations from Ecuadorian network shows a density discrepancy between the Coastal (20 per cent) and the Andean regions (80 per cent).

To avoid the excessive influence of seismic stations on the Andes relative to the Coastal region, we select all available stations on the Coastal region and one on each volcano subnetwork (Fig. 4). The choice of the volcanic station is based on number of records between 1994 and 2007, signal-to-noise ratio and geographic position (preferentially located west of the volcano, to avoid as much as possible velocity structures related to the volcanic edifices). Note that during the hypocentre determination process, only one station at a time can be selected in the groups vc1-mary-tamb and in ara2-retu (Fig. 4). In total, the selected subnetwork is composed of 39 stations.

In addition to the difficulty of the uneven spatial distribution, the performance of the seismic stations on the Coastal area has been intermittent (Fig. 4). Only four coastal stations can be considered as nearly permanent during the 14 yr: jama, hoja, lore, cupa with 13, 12, 12 and 11.5 yr of recording, respectively. Stations magd and sali arrive in second position with 10 and 7 yr of recording, respectively.

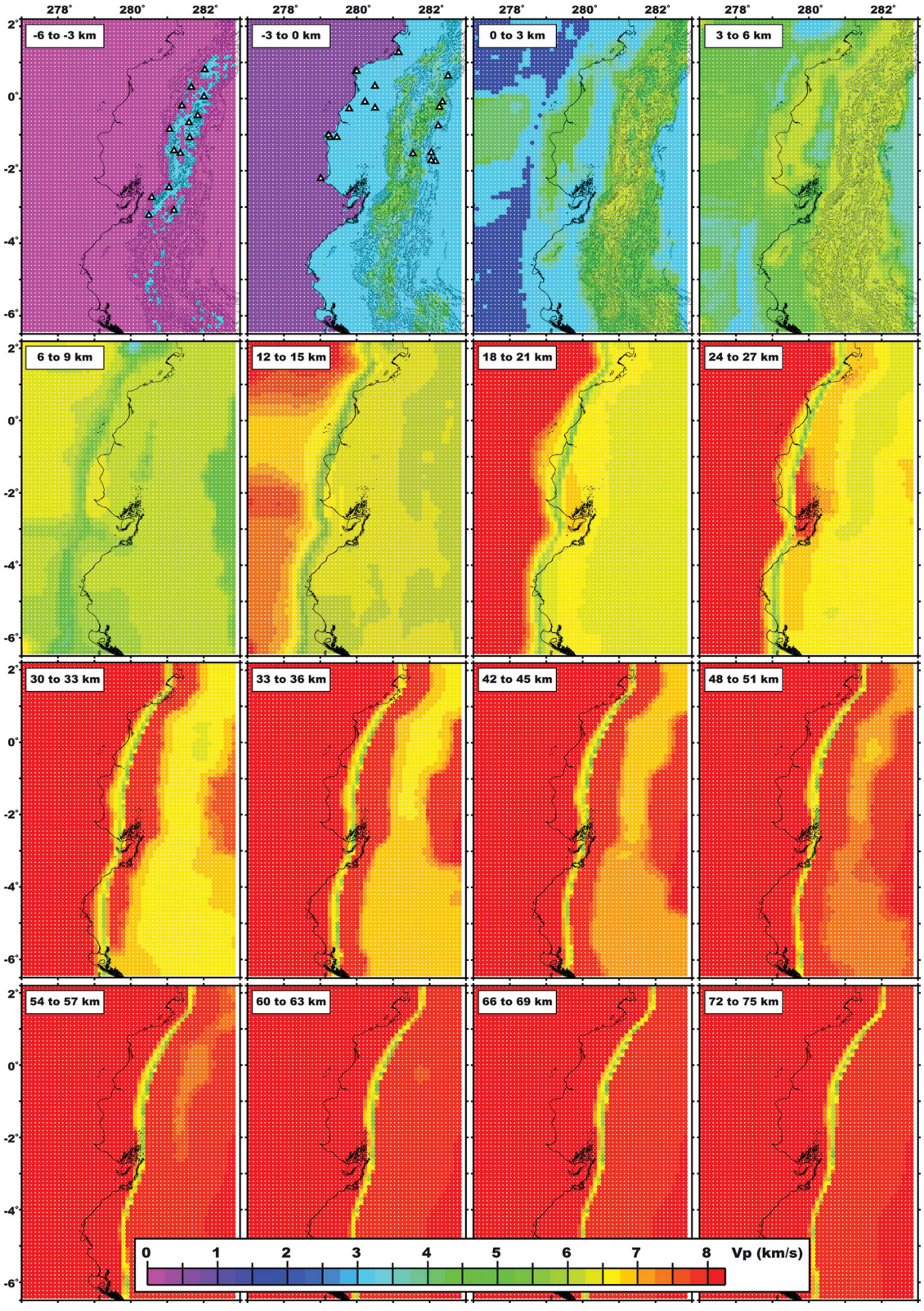

Figure 3. (a) Horizontal and (b) vertical cross-sections showing V_P lateral and vertical variations within the 3-D geo-realistic *a priori* *P*-velocity model (3-DVM) constructed in the study. The 3-DVM is established from the integration of geological and geophysical information collected on the Ecuadorian subduction system. It extends down to 300 km depth. Triangles on both shallower sections represent the position of seismic stations involved in the earthquake location procedure.

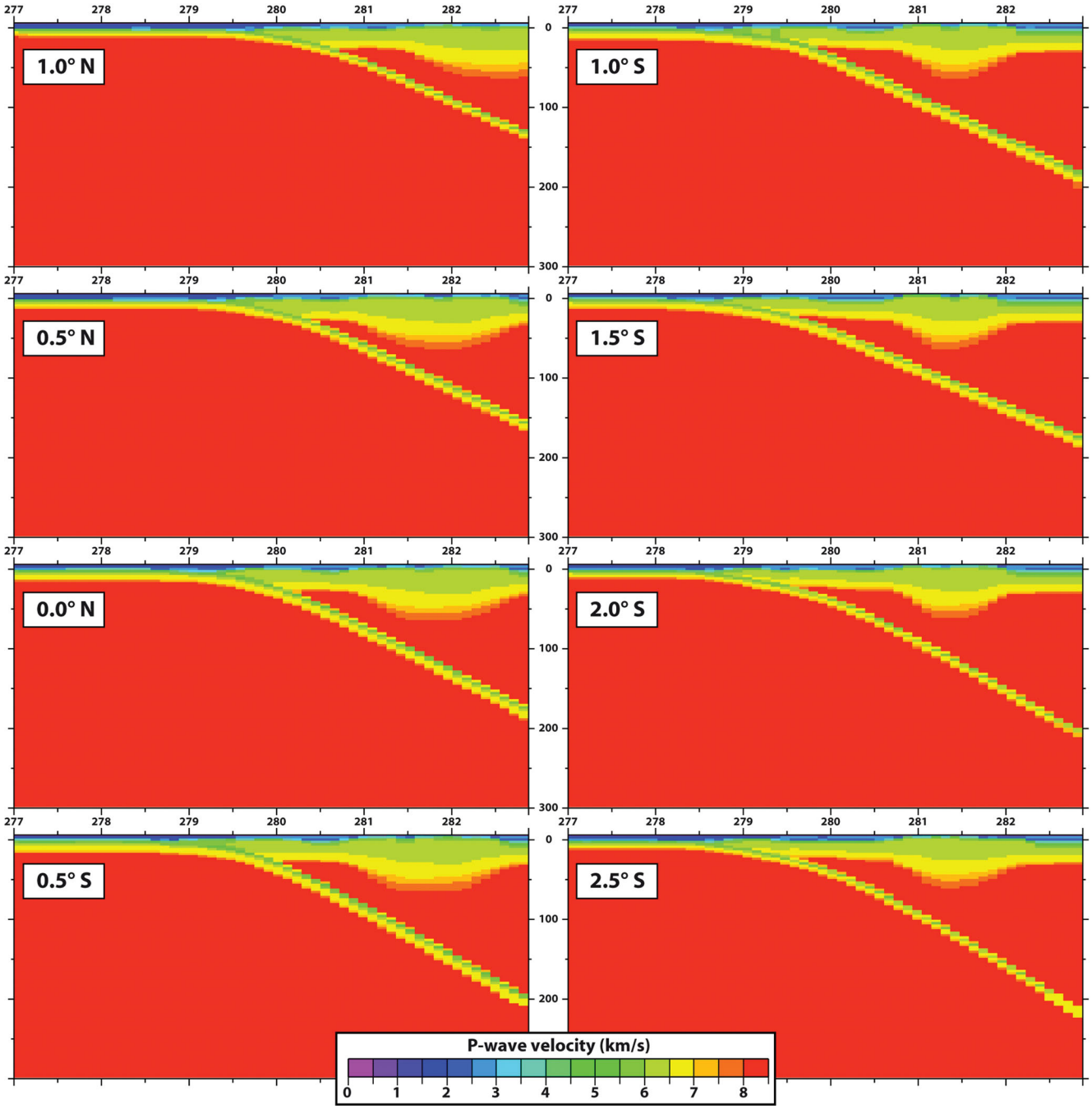

Figure 3 – *continued*

Based on RENSIG hypocentral determinations, five geographical groups share the seismicity distribution as following: 72 per cent of earthquakes are located on the Andean Chain (group A), 6 per cent offshore (group O), 6 per cent on the Coastal Plain (i.e. on the margin between the coast and the western flank of the Andes, group M), 9 per cent south of 2°S (group S) and 7 per cent are deeper than 50 km (group D). Considering only *P* phase arrival times, we select all events that were recorded by at least four seismic stations, among which at least one station belongs to the same geographic group than the event (all available stations for group D). In total, 12 398 events are kept, and 112 148 *P*-wave measurements compose the arrival-time data set.

4 ABSOLUTE EARTHQUAKE LOCATION TECHNIQUE

To search event location within a 3-D medium, we use an updated version of the maximum intersection method. A description of the method and application to the southern Ryukyu seismicity (offshore Taiwan) within a 3-DVM of the region are shown by Font & Lallemand (2009), Font *et al.* (2004) and Theunissen *et al.* (2012). Therefore, only a brief overview of the technique will be given here.

4.1 Maximum intersection technique

MAXI is a direct-search procedure based on graph theory and well adapted to strongly heterogeneous environments. The single event

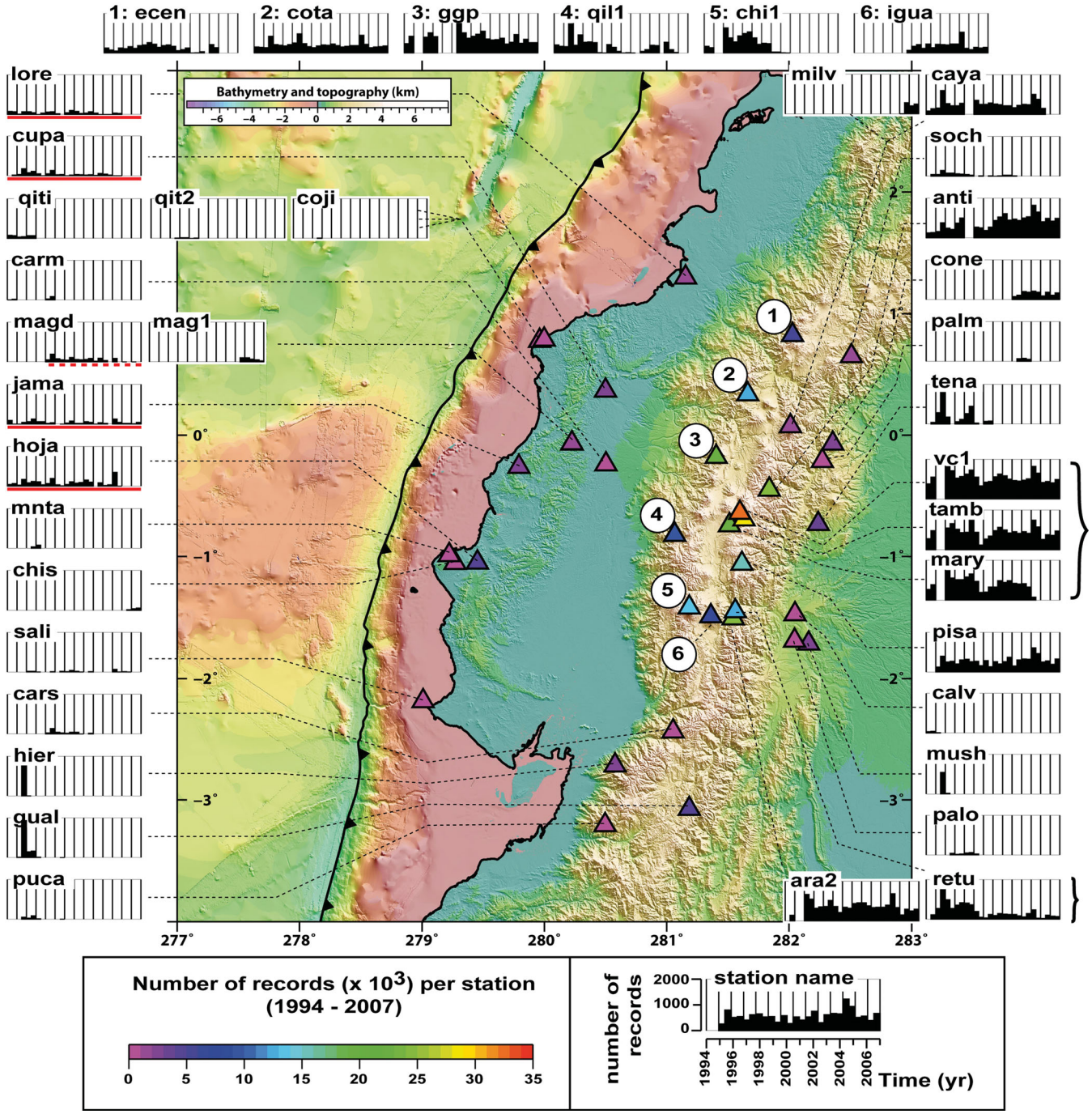

Figure 4. Station map. Triangle = seismic stations selected from the RENSIG network to improve hypocenter determination of the seismicity occurring in the vicinity of the interplate seismogenic zone (subduction front). Triangle colour code: record frequency. Histograms represent the number of *P* arrivals along time (1994–2007). Station positions and associated histograms illustrate the distribution heterogeneity, in space and time, of the permanent network (RENSIG). Bathymetry and topography relief is from Michaud *et al.* (2006).

position is solved by searching for the maximum intersection number of equal differential time (EDT) volumes (Zhou 1994). An EDT volume is described as the collection of grid nodes satisfying the arrival-time difference between two stations ± a tolerance value (in seconds) known as TERR. The node collection organizes in space along a deformed 3-D hyperbolic volume. In a network of j stations, $C_j^2 = \frac{j\times(j-1)}{2}$ EDTs can be constructed and shall intersect around the hypocentral solution. Theoretically, an EDT volume includes the hypocentre. It is important to acknowledge that an EDT volume is totally independent of the earthquake origin time as it only depends on arrival time difference and traveltime computation. Subsequently, from EDT properties, the MAXI search process directly determines the three coordinate parameters (longitude, latitude and depth). The origin-time is then evaluated *a posteriori* once the hypocentre position is solved. Thus, the origin-time estimate does not affect the hypocentre search procedure. Accordingly, except for specific situations, a good approximation of the depth parameter can be achieved using only *P* arrivals (if the 3-D *P*-velocity

model well represents crust and mantle velocity heterogeneities), from the intersections of all possible combination of EDT volumes. The specific situations where the depth unknown can not be well resolved concerns the cases where (1) all stations are at equal distance of the hypocentre, (2) the first arrival is a head wave at all stations and (3) the stations are so far that the curvature of the wave can be neglected. In this study, thanks to the *a priori* station selection that always involves a near-by station, those specific cases should not occur.

For the establishment of the EDT volume, grid nodes are collected by scanning a pre-computed reference file. This reference file stores the ray tracing traveltimes from each node of the dense grid that covers the modelled region to each seismic station. The book-keeping system is strictly identical to the one described by Zhou (1994) who applied the shortest path method (Moser 1991; Moser *et al.* 1992) to compute ray tracings.

The algorithm works as follows. First, an iterative approach on the parameter that controls the EDT thickness (TERR) retrieves a spatial volume (V1) including high-probability solutions, that is all nodes that have been intersected by a maximum number of EDTs at a given iteration. Intersection scores obtained at each iteration are stacked for each node of V1. V1 is then subdivided into two volumes (V2 and V3) in function of the stacked EDT-intersection scores. V3 only includes best-scored nodes and is the smallest volume. V2 contains good-scored node (best intersection-scores minus a confidence margin) and is larger than V3.

Second, a statistical analysis on the EDT intersection rate per seismic station is conducted among V2 nodes to detect and remove inconsistent arrivals from the initial data set. Third, the iterative TERR approach, reconducted within the V4 (i.e. volume expended from V2 to account for grid approximation) on a hierarchy of grid discretization and using cleaned data, better surveys the solution domain and focuses on a small volume (V5) that may include several nodes accounting for the same maximal EDT score. The final absolute hypocentral solution is the barycenter of V5.

Solution reliability of a seismicity data set can be assessed by the analysis of a series of confidence factors and by discarding the determinations presenting statistically extreme values of these factors. Among those, the Q_{EDT} parameter quantifies the ratio between the number of EDTs effectively intersecting the solution and the theoretical maximum number of EDTs involved in the process. Therefore, the Q_{EDT} directly characterizes the consistency between the input data and system parametrization. Q_{EDT} is unitless and varies from 0 to 1. When QEDT is close to 1, one can consider that there is a good consistency between data and system parametrization. In those cases, MAXI confidence factors can also geometrically judge the way a solution is constrained thanks to graphical relations of the solution-node distribution. Two types of factors are considered: (1) size, node density and node distribution of volumes V1, V2 and V3 and (2) spatial coherency of the volumes and their organization in space, which is mainly assessed by the distances between the barycenter of the volumes V1, V2 and V3 (if the distance is too large, volumes do not well superimpose, which suggest multimodal solutions). Each factor taken independently leads to different interpretations and only the combination of a series of factors leads to understanding the location process (see Theunissen *et al.* 2012 for more details).

At last, once the geometrical node distribution is evaluated through the confidence factors, statistical analyses on traveltime residue rms and location uncertainties (based on Sambridge & Kennett 1986) can confirm the reliability of the solution.

Broadly, the main advantages of MAXI is (1) to eliminate the origin time unknown from the search procedure and subsequently to retrieve the depth parameter independently from the origin time, (2) to show good performances when azimuthal coverage is poor, (3) to objectively filter inconsistent arrival times and (4) to be less sensitive to velocity model inaccuracies than techniques that minimize traveltime residues (Theunissen *et al.* 2012).

4.2 MAXI parametrization

The MAXI earthquake location process will search for the solution showing the best consistency between input parameters (such as arrival times, station positions and the discrete 3-DVM) and the parametrization of the system (e.g. grid geometry, TERR variations). A successful search process greatly depends on the parametrization implemented for the velocity grid and the MAXI process, that in turns depend on the network configuration. In this study, because of the seismic stations distribution (∼80 per cent aligned on the Andean Chain), using the MAXI technique by combining all possible pairs of stations provide EDT data sets that (1) are spatially tangent (approximately normal to the trench) when focusing on offshore earthquakes and (2) enhance the velocity anomalies not taken into account beneath active volcanoes.

To avoid these difficulties, we limit the number of EDT volumes to the set of pairs that include the station with the earliest arrival time. For an earthquake recorded by j stations, $(j-1)$ EDTs are thus used to determine the solution (at a given TERR value). This choice gives more weight to the first station and its surrounding velocity model, in the sense that all EDTs rely on the first station arrival time and are combined only once with the remaining stations, thus reducing the harmful effect of structural anomalies under the volcanic arc. Consequently, this choice is particularly advantageous for the location process of earthquakes occurring offshore or near the coast. However, it should be noted that if the first arrival is erroneous, the hypocenter determination will be shifted in space (Font *et al.* 2004).

Based on the grid parametrization and on classical estimations of picking errors for regional earthquakes (Zeiler & Velasco 2009), we implement the TERR parameter (that controls the thickness of EDT) to increase from 0.4 to 0.8 s with an increment of 0.1 s. The initial node spacing is defined above; the secondary grid is composed of nodes equally spaced and distant of 0.5 km.

5 SYNTHETIC RESOLUTION INVESTIGATION

The configuration of seismic station in Ecuador between 1994 and 2007 is not constant through time and only includes a few coastal stations. To evaluate the ability of the selected subnetwork to properly locate subduction earthquakes using *P* arrivals and the MAXI technique, we design a synthetic investigation aiming to mimic the realistic azimuthal gap and 3-D configuration.

The first step consists in retrieving 3-D synthetic *P*-wave arrival times, with the objective to simulate the acquisition of seismic waves that propagate within a strongly heterogeneous medium. To do so, we extract all earthquake positions from the initial RENSIG data set (∼12 400 events). From a known event position, we retrieve the 3-D traveltimes applying the ray tracing shortest path method (Moser 1991) within the 3-DVM, and using a fixed origin time, we establish the synthetic arrival time. Synthetic arrivals are only restored at the station positions that genuinely recorded the earthquake to re-create the network conditions at the time of the recorded event.

Table 1. Synthetic investigation results or study feasibility. The event distribution (in per cent) is classified per intervals of misfit (the misfit being the distance between the hypocenter solution and the initial event position). Each column refers to a specific geographic group; the number of events is given in the second line of each column. In the best conditions of a known velocity model and exact *P*-waves arrival times, the application of the MAXI technique using the spatial-and-temporal distribution of *P*-arrivals within the 3-DVM resolves ∼70 per cent of hypocenter determination offshore Ecuador with less than 5 km of error.

	Andes	Deep	South	Margin	Offshore
	5470	1778	1843	1447	1860
00 < misfit < 05 km	90.3	80.4	69.2	57.2	67.5
05 < misfit < 10 km	5.2	12.5	20.3	20	18.4
10 < misfit < 15 km	1.2	2.9	6.6	10.7	6.5
15 < misfit < 20 km	0.5	1.8	1.4	4.6	3
20 < misfit < 50 km	0.3	1.4	1.9	5.5	2.2
Misfit > 50 km	0.2	0.2	0.3	0.3	0.2
No solution	2.3	0.8	0.3	1.7	2.2

Second, we search for the absolute earthquake positions using the exact 3-D synthetic arrival data set, the 3-DVM and the MAXI technique. Grid and technical parametrizations are identical to those described in the previous paragraph and that are also used for the real-case application.

The accuracy of earthquake location for the synthetic experiment is recovered by the statistical analyses of the misfit, defined as the distance (in kilometres) between the final solution and the initial synthetic event position. The efficiency of the 3-D approach and network configuration is assessed through the hypocenter determination accuracy. The average misfit per geographic group (A, D, M, O and S) and per misfit interval is shown on Table 1. As expected, in broad approximation, mislocation increases when earthquakes occur far outside and off the seismic network. In group A, 96 per cent can be determined with less than 10 km of error while 93 and 90 per cent characterize group D and S, respectively. Nevertheless, 77 and 86 per cent of events can still be determined in groups M and O, respectively, with less than 10 km of error, even though source-to-station distance and azimuthal gap increase.

The statistical analysis on the misfit values and the spatial repartition for synthetic events of group M and O (Fig. 5) reveals that, under the best conditions (i.e. when the 3-DVM and arrival times are perfectly known), ∼2085 among 3300 events can be accurately located (with a misfit <5 km; ∼2700 events with less than 10 km of error). The average misfit for the whole event data set is 5.5 km (±7.1) km, with dx, dy, dz reaching respectively −0.5 (±4.2) km, 0.1 (±1.9) km and 2.4 (±7.4) km. Note that the spatial position of the synthetic events does not seem to influence the misfit as the earthquake distribution covers the same area whatever the misfit range. Considering the network aperture, the azimuthal gap for events of group O associated to a misfit lower than 5 km is, on average, 289° (±44°). The azimuthal gap average roughly increases by 40° from small (<5 km) to large (>50 km) misfit values for group O, and by ∼10° for group M (Fig. 5). However, while the average increases, the dispersion of azimuthal gap values around the average is large (± 40 and ± 60° for group O and M, respectively). Consequently, location error cannot be directly related to poor azimuthal gap.

The noise-free synthetic investigation indicates that, within an exact 3-D *P*-velocity model, the spatiotemporal configuration of the network is appropriate enough to accurately locate a reasonable percentage of earthquakes in the frontal part of the subduction zone. For a more realistic test, we introduce some noise into the 3-D synthetic arrival times and perform earthquake location following the exact same procedure (Fig. 6). The disturbance follows a Gaussian distribution between +/− 0.3 s. Allowing for noise in the arrival time data set decreases the quality of hypocenter determinations. Still, 51 per cent of the events from group O and M have a misfit lower than 10 km (1050 events with less than 5 km error).

The last test reproduces the synthetic experiment (with exact 3-D arrival times) but processing earthquake location within a 1-D velocity model. The 1-D model is taken from the RENSIG (Table 2) and is projected on the same grid parametrization than the one used in the 3-D case. The classification of the results per range of misfit (Fig. 7) is shown for comparison with 3-D experiment (Fig. 5 or 6). The results confirm that, for the Ecuadorian subduction configuration, processing earthquake location within a 1-D-velocity model almost never allows accurate hypocenter position for offshore earthquakes. This experiment highlights the damaging impact of traveltimes computed in a 1-D medium when seismic rays have indeed travelled into a heterogeneous medium and enhances the importance of a realistic velocity model.

The synthetic tests shown here validate the legitimacy of the 3-D approach proposed in this paper, that is the joint use of *P* arrivals and the MAXI technique, especially because no detailed tomography exists. The azimuthal gap dispersion observed for events associated to small misfits lead us to avoid an *a priori* selection of data as a function of gap. Therefore, the whole data set of 12 398 events is used in the real application.

6 ABSOLUTE HYPOCENTER DETERMINATION: PROCESSING, RESULTS AND COMPARISON

6.1 Processing

The application to the real case involves three steps. The two first steps consist in identifying incorrect stations and evaluating station correction terms. The last step consists in locating the earthquake data set applying static station delays to integrate velocity model errors under each station.

First, the *P* arrivals selected from the 14-yr long RENSIG catalogue are used to locate the 12 400 events, using MAXI (and the parametrization described previously) within the 3-DVM established for whole Ecuador. All 39 seismic stations from the selected subnetwork are used. To evaluate static station terms, we analyse the resulting phase outputs for preliminary hypocenter solutions (i.e. before removing inconsistent arrivals from the initial data set). The MAXI technique produces two types of information for each phase involved: (1) EDT-intersection rate per phase (i.e. per station, because in this case only *P* arrivals are taken into account) and (2) traveltime residual per station. Because of the choices in MAXI procedure (i.e. all EDTs are only combined to the first arrival), we separate information associated to 'a first station' from the others (that we will call later on 'the remaining phases'). The reason for this separation is that *first station* traveltime residuals are predictably very small and meaningless for static term recovering. Based on the remaining phases, we distinguish, in terms of EDT-intersection rate per station, EDT-in phases from EDT-out ones. Phases qualified as EDT-out are arrival times whose associated EDTs do not cross the solutions. By extension, we call EDT-in the phases associated to EDTs that do cross the solution. This distinction allows us to objectively and statistically evaluate the phases that are inconsistent with the remaining set of data.

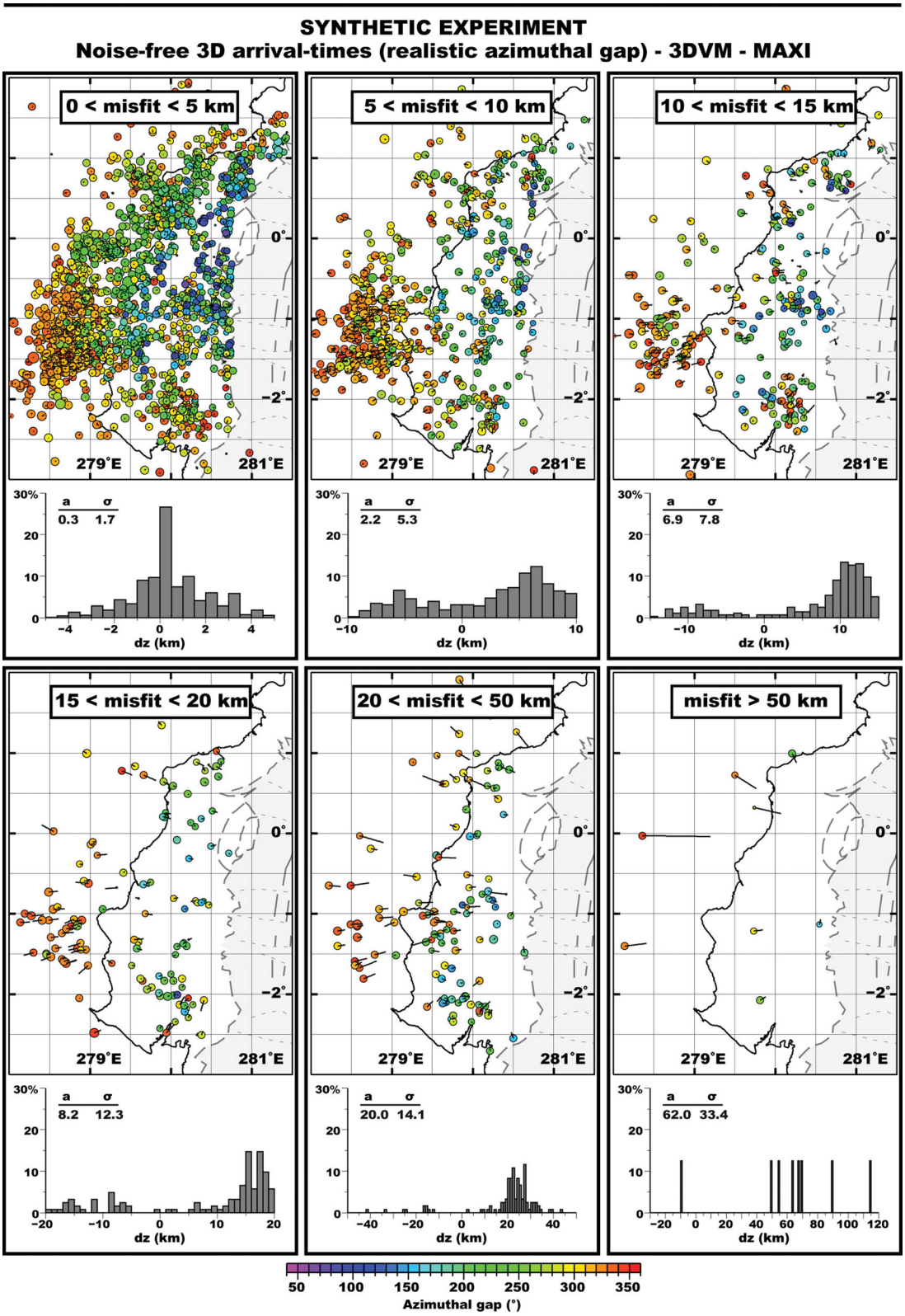

Figure 5. Noise-free synthetic experiment to examine the ability of the network (and its spatiotemporal heterogeneity) to solve earthquake locations for events of group O and M (*Offshore* and *Margin*) within the 3-DVM. Initial event position (empty side of the stroke) is from the RENSIG. Synthetic 3-D *P*-wave arrival times are retrieved with the genuine azimuthal gap. The parametrization of the MAXI technique and 3-DVM grid is identical to the application to real data (see text for more details). The circles represent hypocenter solutions; the colour code indicates the azimuthal gap. Each map corresponds to a given misfit range (see also Table 2). Below each map, the associated histogram evidences the absolute depth difference between the initial event and the solution (normalized on the number of events involved in each range). The synthetic investigation suggests that the network spatiotemporal configuration is appropriate to resolve 70 per cent of earthquake locations offshore Ecuador.

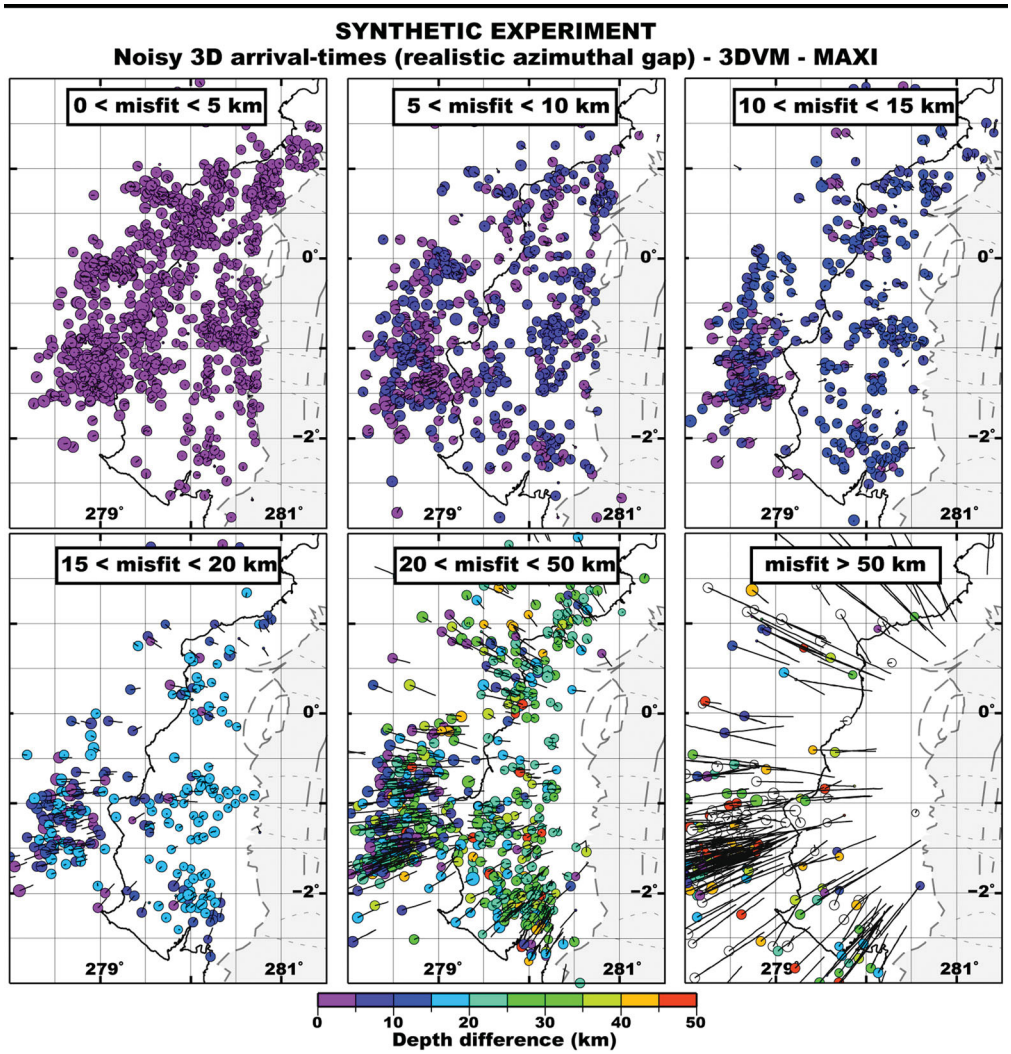

Figure 6. Same as in Fig. 5 except that 3-D synthetic *P* arrivals are disturbed with noise (following a Gaussian distribution between ±0.3 s). The circle colour code indicates the absolute depth difference between the initial synthetic event and the 3-D solution. The synthetic investigation suggests that, considering noisy arrivals, the network's spatiotemporal configuration is appropriate to resolve 50 per cent of earthquake location offshore Ecuador.

Table 2. 1-D velocity model (named ASW) used for the RENSIG hypocenter determinations. The depth of the each layer top limit is given with respect to the sea level.

V_P (km s^{-1})	V_S (km s^{-1})	Layer depth (km)
3.32	1.94	3.30
5.90	3.45	0.30
6.20	3.63	−11.70
6.70	3.92	−26.70
8.10	4.74	−46.70

Analysing EDT-intersection rate per station, 37 stations out of 39 are qualified as EDT-in at 86 per cent (on average), indicating that those stations create, by combination with whatever other station, EDTs that do intersect the hypocenter determination 86 per cent of the time. Both remaining stations (ecen and carm; Fig. 4) are EDT-out at 98 and 90 per cent (with ∼1000 and 100 arrivals for ecen and carm, respectively), which mean that EDTs associated to both stations almost never intersect the hypocenter determination. Residual averages reach nearly −8 and −2 seconds for ecen and carm, respectively.

In the second step, we relocated all seismicity using 37 stations, including ecen and carm only to retrieve residual values (but without using the stations in the search process). We then computed static station corrections following the same event data separation as explained above. The residual statistic analysis is conducted separately for each geographic group of events (Andes–A-, Margin–M-, Offshore–O-, South–S- and Deep–D-). Note that the rms of the residual distribution are small and never exceed 0.2 s, even for the stations ecen and carm, attesting that traveltime residuals are distributed according to narrow Gaussians. Residual averages for stations ecen and carm are about −7 and −1 s (Table 3), which suggests that, in the first location trial, EDTs from the stations ecen and carm did affect the hypocenter solutions. From the sharp shape of the Gaussian distribution, we consider that some velocity anomalies under the stations had not been taken into account within the 3-DVM, except for station ecen whose large residual average is not easily explained except by a station mislocation or a timing error. Static term values are reported in Table 3. All values are relatively small.

The third stage relocates all seismicity, separated per geographic group of events, applying the corresponding station corrections.

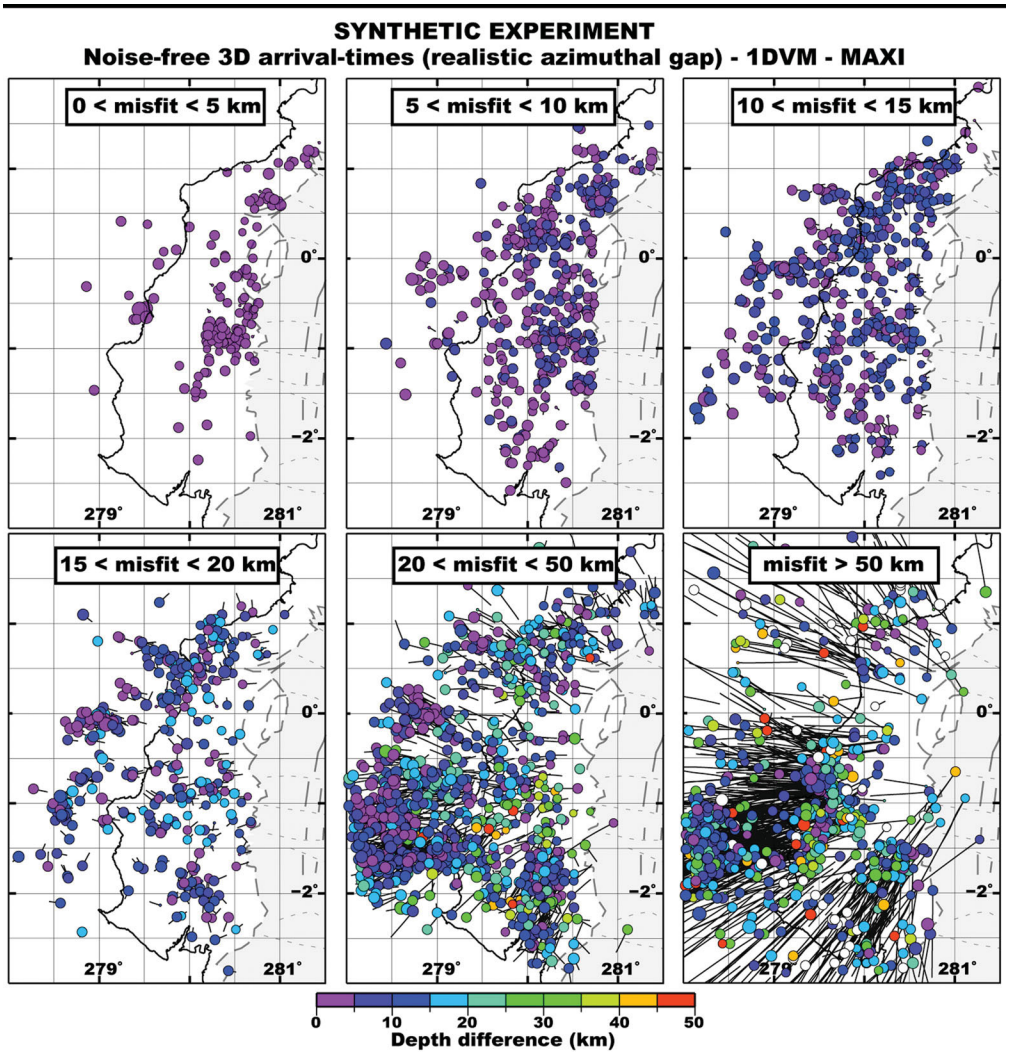

Figure 7. Same as Fig. 5 except that the 3-D synthetic *P* arrivals are used within a 1-D velocity model (from the RENSIG). The circle colour-code indicates the absolute depth difference between the initial synthetic event and the solution. The synthetic investigation suggests that a 1-D velocity model can only resolve 15 per cent of earthquake location offshore Ecuador.

To obtain a high quality data set, we select earthquakes based on MAXI confidence factors: (1) Qedt $\geq$ 0.6 (2) interbarycenter distance (between volumes V1 and V2; see section 4.1) <15 km (3) distance to first station <200 km and (4) number of V2 solution nodes <1000 (see section on MAXI technique). After quality selection, the Qedt average is 0.94 ($\pm$0.07), the average residual rms is 0.21 ($\pm$0.13) s, the average number of stations is 7.7 ($\pm$2.0, and the average location uncertainties dx, dy, dz are 1.5 ($\pm$2.1 km), 1.2 ($\pm$1.9 km), 1.4 ($\pm$1.8 km), respectively. Finally, our catalogue is composed of 7950 earthquakes with a quality considered as high (Figs 8 (zoom) and 9a).

6.2 Results

Because hypocenter location uncertainties are generally underestimated (Billings *et al.* 1994; Shearer 1997), earthquake location quality can be assessed from seismicity clustering or alignment along well-known tectonic features. We thus will succinctly describe the seismicity observed at the vicinity of the interplate seismogenic zone and compare them to 1-D hypocenter determinations.

To the north, near 0.5°N (near the town of Muisne; Fig. 1), a 60-km-long alignment of earthquakes narrowly spreads ~NW–SE, perpendicular to the trench, 15 km landward from the trench to 20 km inland from the coast line (Figs 8 and 9a). This seismic pattern is known as the *Galera alignment* (Segovia 2001). Hypocenters mainly occur from about 10 to 30 km depth, along a plane dipping gently eastward, most probably the interplate seismogenic zone (Fig. 8—section 1). Seismicity also scatters within the overriding crust and, in less proportion, within the subducting plate.

Southward, near 0.25°S, a cluster of earthquakes occurs at about 10 km landward from the trench, extending over about 35 km of distance. At depth, this cluster (further on referred to the *Jama cluster*) essentially affects the overriding plate down to the presumed plate interface (dipping 10° towards the east). The interplate activity is bounded between 8 and 14 km depth. Locally, a small amount of seismic activity takes place deeper within the bending slab (beneath the trench) between 30 and 80 km depth (Fig. 8—section 2).

To the south, centred on 1.25°S, seismicity recurrently strikes the margin through large seismic swarms. This cluster (further on referred as the *Manta cluster* after Vaca 2007) extends along 90 km, in a direction parallel to the trench and 15–20 km landward from it. At depth, seismicity concentrates in the overriding plate down to the plate interface (Fig. 8—section 3).

Table 3. Station corrections, in seconds, computed at each station of the selected subnetwork from the 3-D approach statistical investigations (see text for more details). Station location is shown on Fig. 2. Bold font highlights stations *ecen* and *carm*, qualified as EDT-out (98 and 90 per cent, respectively).

	A	D	S	M	O
anti	0.19	0.06	0.16	−0.04	−0.11
ara2	0.07	0.11	0.33	0.00	−0.06
calv	−0.11	0.02	0.00	0.00	0.00
cars	−0.01	0.04	0.00	0.07	−0.02
caya	0.05	−0.03	−0.14	−0.06	−0.06
chi1	−0.16	−0.01	−0.26	0.16	0.20
cone	−0.28	0.08	−0.11	−0.19	−0.07
cota	−0.07	0.04	0.10	0.09	0.15
ecen	**7.23**	**7.09**	**6.64**	**7.23**	**7.67**
ggp	0.17	0.09	−0.14	0.14	0.27
igua	0.19	0.18	0.04	0.13	0.22
mary	−0.09	0.06	−0.01	−0.14	−0.01
milv	0.18	−0.04	−0.16	−0.08	−0.18
mush	0.34	0.00	0.72	0.00	0.00
palm	−0.24	−0.17	−0.09	0.00	−0.25
palo	0.10	0.03	0.12	−0.04	0.00
pisa	−0.03	−0.18	0.15	−0.22	−0.24
qil1	0.01	−0.02	0.12	0.19	0.21
retu	0.07	0.17	0.05	0.14	0.03
soch	−0.10	0.04	−0.19	−0.07	−0.03
tamb	−0.17	0.07	−0.09	0.08	−0.19
tena	−0.17	0.05	−0.05	−0.04	0.03
vc1	−0.22	−0.10	−0.12	−0.16	−0.15
carm	**0.74**	**1.27**	**0.00**	**1.86**	**1.81**
chis	0.00	0.02	0.00	−0.08	0.16
coji	0.00	0.00	0.00	0.00	0.03
cupa	−0.14	−0.15	−0.19	−0.06	−0.04
hoja	−0.11	0.02	−0.14	0.08	0.06
jama	0.12	0.05	0.10	0.10	0.13
lore	0.01	−0.13	−0.54	−0.07	−0.08
mag1	−0.11	−0.18	0.03	0.15	0.03
magd	−0.15	−0.04	0.14	0.00	−0.22
mnta	0.04	−0.02	0.19	−0.01	−0.05
qit2	−0.15	−0.09	0.00	−0.14	0.10
qiti	0.08	−0.06	−0.29	−0.11	0.07
sali	−0.28	−0.11	−1.41	0.11	0.06
gual	0.02	−0.08	0.18	0.02	−0.01
hier	−0.10	0.07	−0.11	0.21	0.81
puca	−0.16	0.20	0.06	−0.07	−0.08

The Jama and Manta clusters and their depth distribution near the expected interplate seismogenic zone are consistent with the seismic activity known in other subduction zones. In addition, given that each earthquake is located independently, the tightness of the Galera alignment tends to support the notion that in addition to reliable confidence factors and uncertainty parameters hypocenter determinations resulting from the proposed 3-D approach are reasonably accurate.

6.3 Comparison to 1-D-determinations

To assess the effect of the 3-DVM in earthquake location (real data application), we perform hypocenter determinations using a procedure identical to what is presented above (same *P*-wave arrival data set and MAXI technique) but implemented within the same 1-D velocity model than the one used by the *Instituto Geofisico*. We name MAXI-1-D the resulting hypocenter determinations. The MAXI-1-D catalogue includes the same events as MAXI-3-D. The 1-D model used by *Instituto Geofísico* was constructed based on the Andean geology and is used indistinctly in all the country (Table 2).

Based on the MAXI-1-D results, the Galera alignment is barely recognizable. At this latitude, the Galera seismicity seems to start about 30 km landward compared to MAXI-3-D results (Figs 9 and 10). The depth distribution shows two distinct clusters. The deeper one is extending from 10 to 50 km depth, the shallower strikes in part in the air and sea water and affects essentially the overriding margin. The Jama cluster epicentral position scatters east and west from the trench. Depth determinations range between –5 km (west of the trench) to 40 km depth (at 80 km landward from the trench), affecting essentially the crust and mantle of the subducting plate. The Manta cluster is also scattered and separates in two groups with a distance of ∼20 km. The northern one extends from 20 to 30 km west of the trench to near the coastline, occurring to a large degree within the water column. The southern one is located at less than 10 km from the trench and spread to the coastline. Seismicity deepens with sea water depth, near and around the seismogenic plate interface, down to about 30 km depth.

To assess the effect of the location technique, we evaluate MAXI-1-D against RENSIG determinations. Note however, that this latter comparison is not totally appropriate because the RENSIG uses *P* and *S*-wave arrival times on the whole network. RENSIG determinations are performed using the 1-D-layered model described above and the FASTHYPO technique (Herrmann 1979) which minimizes traveltimes residuals similar to other location programs. This algorithm was modified locally to consider stations delays because of high altitude variations of some seismic stations.

From the RENSIG determinations, the Galera alignment is clearly visible. It initiates 10 km before trench and extends to the coastline. Seismicity occurs at 30 km depth beneath the trench and continuously affects the crust and mantle of the subducting plate (between 20 and 45 km depth). Very little activity appears at the interplate seismogenic zone or in the overriding plate. The Jama and Manta clusters are both relatively well clustered and occur on both sides of the trench. Both cluster seismicity delineates, at depth, a ∼20 km-thick plane dipping eastwards with an angle of about 20-to-25° (when starting from the trench). The activity stops at 35 km depth, for the Jama cluster, and near 30 km depth for the Manta cluster.

6.4 Effect of the *a priori* 3-D velocity model

The velocity model errors have been found to have a larger effect on location procedure than the effect of picking errors (e.g. Gomberg *et al.* 1990; Billings *et al.* 1994; Husen *et al.* 2003; Bai & Greenhalgh 2006). As the real heterogeneity of the crust and mantle is rarely well known, this conclusion mainly results from synthetic investigations and the common knowledge that a 1-D model cannot account for complicated velocity structure. Indeed, in real applications, at local to regional scale and in well-instrumented region, 3-DVM obtained from tomographic inversion of local earthquakes (starting from a minimum 1-D velocity model and associated 1-D-hypocenter determination) only produces a few differences in earthquake location, with no large systematic shift but an clustering of seismicity and slight depth variations (< 3 km, in average, given by Micheal 1988; Husen & Smith 2004). On land, a probabilistic earthquake location in Switzerland and the integration of *a priori* knowledge in the 3-DVM generates large individual shifts but there were not systematic (Husen *et al.* 2003). In this study, the velocity model is totally constrained from *a priori* knowledge. Its adequacy to represent locally the earth structure can be appraised from formal

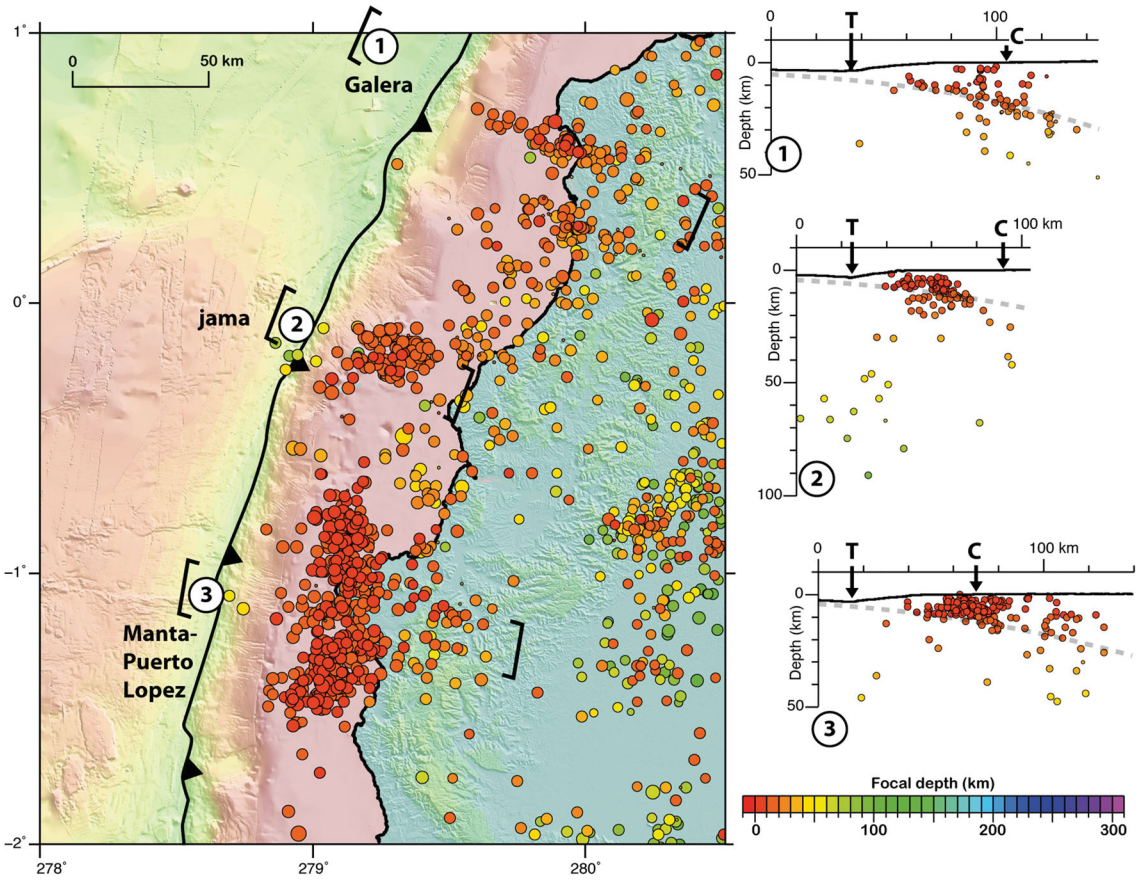

Figure 8. Seismic hypocenter location map and cross-sections in the vicinity of the interplate seismogenic zone: results from the 3-D approach and *P*-wave arrivals. Section 1 refers to the Galera alignment, 2 and 3 to Jama and Manta clusters, respectively. Section locations and width appear as brackets on the map. Bold line with triangles is the trench.

earthquake location uncertainties, traveltime residual statistics per seismic station (Table 3) and the geological reasonableness of the seismicity distribution.

The effect of the 3-DVM on earthquake location can be assessed by comparing MAXI-3-D and MAXI-1-D results (application to real data; Figs 9 and 10). The distances between 1-D and 3-D-resolved hypocenters are in average 36 ± 23 km (dx = 7 ± 35 km, dy = 7 ± 16 km and dz = 4 ± 15). As the only difference between both catalogues is the velocity model in which ray paths propagate, the differences in earthquake position directly illustrate the effect of the differences in traveltime estimates between 3-D and 1-D models (see Table N2-old3, for 1-D model). First, we observe that this effect is not systematic (Figs 9 and 10). Relatively to MAXI-3-D, the earthquake position of the Galera alignment tends to move land ward while a good proportion of Jama and Manta earthquakes are moving seaward. The depth parameter also undergoes a non-systematic shift, deeper along the Muisne alignment and shallower for the western part of Jama and Manta clusters. Second, even though the 3-D approach handles single-event locations, epicenters appear to better cluster. Third, even if the real hypocenter position is not known, the MAXI-3-D evaluation of depth (more consistent with the plate interface) also appears more realistic than MAXI-1-D (Fig. 10). Consequently, despite that the quality of the 3-DVM is not directly evaluated as it would be in a tomographic inversion, its implementation produces an image of seismicity that seems more reliable.

In seismology, assessing the reliability of hypocenter determinations is challenging because location uncertainties are generally underestimated and because uncertainties depend on the velocity model in which the solution is produced (Sambridge & Kennett 1986; Billings *et al.* 1994; Shearer 1997). In addition to the high values of the confidence indicators and small uncertainties, the MAXI-3-D seismicity appears to be reliable because it is consistent with the plate interface location in the vicinity of where one expects seismogenic deformation and because its clustering in space conveys the image of seismic activity on a portion of a fault. As a first approximation, we therefore consider that the 3-DVM established to represent velocity variations in the area is trustworthy and advantageous for earthquake location.

In this study, we have constructed the V_P 3-DVM with care. Nevertheless, initial data on crust and mantle velocity properties do not uniformly cover the studied area and some necessary information is uncertain or missing (for instance, the forearc crustal thickness lacks recent constraints; magmatic chambers are not taken into consideration). Therefore, the 3-DVM most certainly only approximates to first order the large-scale velocity variations. If non-existent local heterogeneities might be introduced by mistake in the 3-DVM, we assume they are insignificant compared to large scales anomalies that a 1-D layered model would inexorably generate when trying to represent a non-flat configuration of crust and mantle such as in subduction zones. In such areas, 1-D-layered velocity model obviously degrades traveltime computations and thus earthquake location accuracy. Consequently, in subduction zone seismological studies, exploration of the concept of *a priori* 3-D velocity models and questioning the classical 1-D-approach seem fully appropriate.

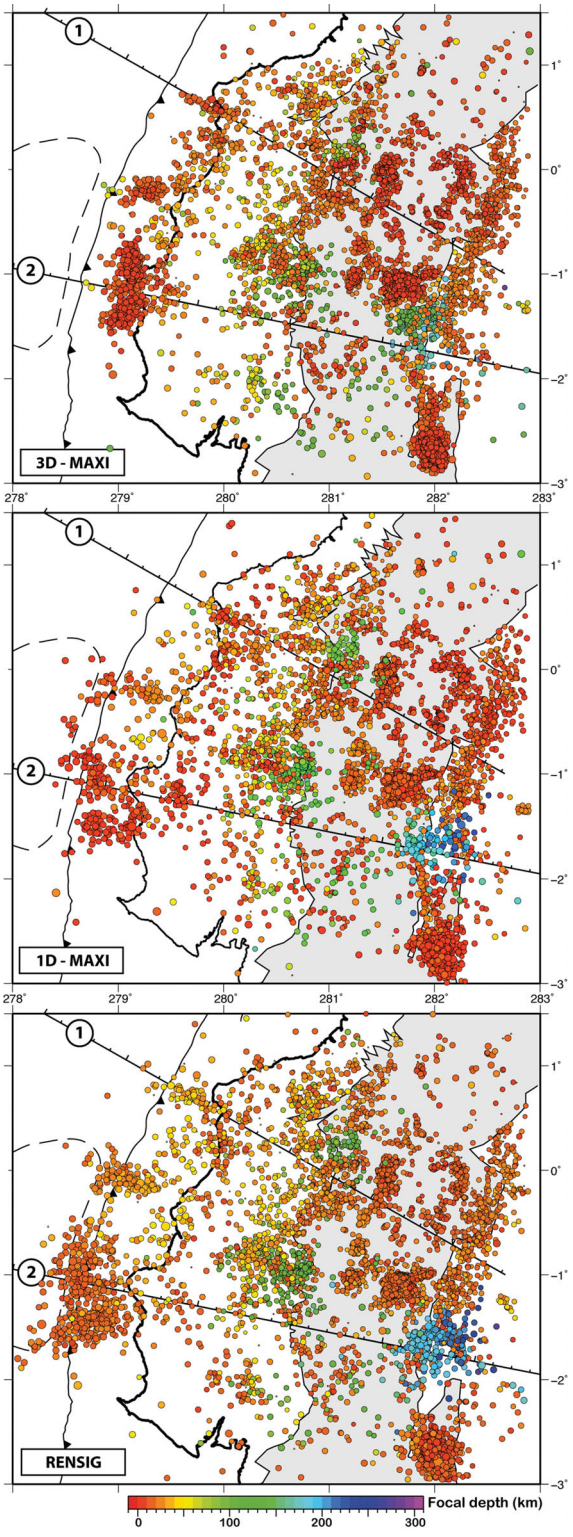

Figure 9. Seismicity map comparing earthquake location resulting from three different procedures. 3-D-*MAXI* refers to the catalogue resulting from earthquake location using: a selection of RENSIG stations, *P* arrivals, 3-DVM, and the MAXI technique (see text for more details). 1-D-*MAXI*: identical procedure within a 1-D-layered model (from the RENSIG). *RENSIG* refers to the whole network, *P*- and *S*-waves arrivals, 1-D-layered model (see Table 3) and FASTHYPO (Herrmann 1979). The traces of the Carnegie Ridge (dashed line), the trench (bold line and triangles) and the Andean Chain (in grey) are marked for references. 1 and 2 identify the cross-section shown on Fig. 10.

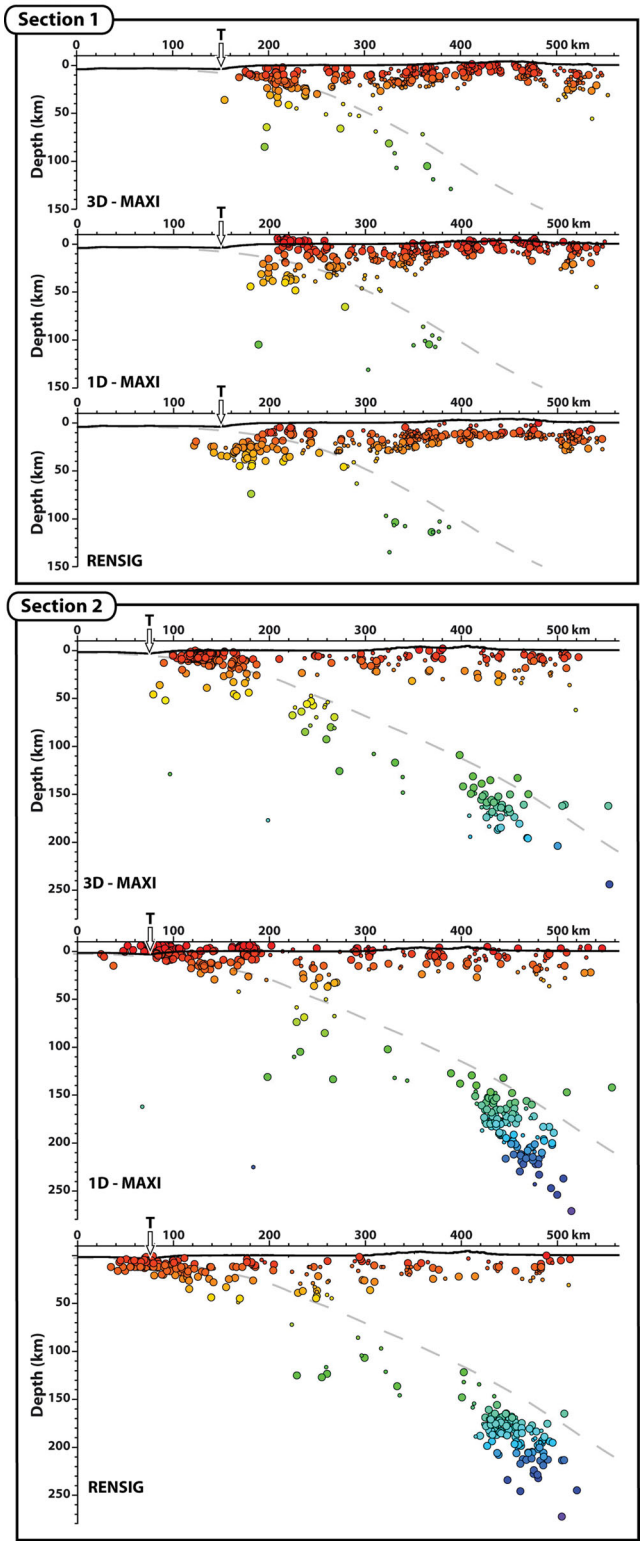

Figure 10. Seismicity cross-sections comparing earthquake location resulting from three different procedures (location on Fig. 9). See Fig. 9 for explanations about 3-D-*MAXI*, 1-D-*MAXI* and *RENSIG* procedures. The grey dash line marks an eventual position of the Nazca Plate top and serves as spatial reference.

A second question concerns the use of an unconstrained *S*-wave velocity model in earthquake location because, from what is said above, the accuracy of the velocity model mainly controls the quality of earthquake location. Indeed, *a priori S*-wave velocity models are not available if tomographic inversions cannot be performed. Furthermore, when tomographic investigations can be performed in subduction zones, it is observed that the V_P/V_S ratio is far from constant in those systems because of the high fluid content and fracturing (e.g. DeShon *et al.* 2006). Variations of V_P/V_S ratios are also in receiver function investigation (e.g. Audet *et al.* 2009). In addition, relatively to *P* arrivals, measuring *S*-wave arrival times is complicated by the *P*-wave coda and conversions. Zeiler & Velasco (2009) reported that, at local to regional distance range (0°–30°), most of the picking errors were associated with the *S* and S_g phases. By comparing common arrival times reported by several institutions, they demonstrate that the average time difference for *S* waves reached 5.5 s (compared to 0.4 s for *P* waves). Zeiler & Velasco (2009) also indicate that short-period instruments are not as precise when used to pick arrivals. In the specific case of Ecuador, most stations of the permanent network are composed of vertical component short-period sensors, which are known to distort the *S* arrival-time measurements. Subsequently, the *S* measurement precision should be considered as suspicious (compared to *P* arrivals), and most probably flawed in the specific case of Ecuador (mainly because of the network characteristics).

Given those difficulties, one can wonder what would be the effect of a non-precise *S*-velocity model and inaccurate *S* arrivals in the process of earthquake location. The answer to this question certainly depends on the relative quality between the *S* and *P* velocity model. Although beyond the scoop of this paper, synthetic investigations should be carried out using heterogeneous models and arrival-time difference technique to bring some answers on the effect of a biases *S*-velocity model on earthquake location. In this study investigation, because of the inferred large heterogeneities of crust and mantle, the unknown quantity of water in the mantle wedge, the geometry and positions of magmatic chambers, the lack of information on fracturing, and the uncertain quality of *S* arrival times, we favour the use of a unique *P*-velocity model. It is worth noting that, whereas most seismologists commonly use both *P* and *S* waves, some local to regional studies provide interesting results using *P* waves only (e.g. Husen *et al.* 2003; DeShon *et al.* 2007; Arroyo *et al.* 2009).

7 SEISMICITY PATTERN WITHIN THE INTER-SEISMIC PERIOD ALONG THE ECUADORIAN SUBDUCTION ZONE

7.1 Historical earthquakes known along the northern Ecuador subduction zone

In 1906, a $M_w = 8.8$ megathrust earthquake, accompanied by a large far-field and local tsunami, ruptured the subduction fault zone in North Ecuador South Colombia along a 500-km-long rupture area (Kelleher 1972; Kanamori & McNally 1982). The epicenter of this event was first located seaward from the trench (Gutenber & Richter 1959), but from constant (*S–P*) time at teleseismic stations (Baltimore and Victoria, Kanamori & McNally 1982) and from the intensity distribution described by Rudolph & Szirtes (1911), we prefer the epicenter position from Collot *et al.* (2004) near 0.8°N and 280°E (Fig. 11). Much of the rupture zone that broke during the 1906 event ruptured again, with thrust motion, during the $M_w = 7.9$ earthquake of 1942, the $M_w = 7.7$ 1958 earthquake and the $M_w = 8.2$ 1979 earthquake (Kanamori & McNally 1982; Mendoza & Dewey 1984; Swenson & Beck 1996). The rupture zones of the three smaller events (1942, 1958 and 1979), approximated from the distribution of aftershocks, abut closely without significant overlap. In the study area, the 1942 epicenter has been located near 0°S and 279.8°E (Kelleher 1972; Swenson & Beck 1996; Engdahl & Villaseñor 2002). Its rupture zone propagated from south to north (Kelleher 1972; Mendoza & Dewey 1984, Fig. 11). The source–time function of this event is characteristics of a single asperity rupture (although its location is uncertain), and most of the seismic moment is assumed to be released within approximately 50 km of the epicenter (Swenson & Beck 1996). The original rupture zone extends westwards from the trench. In Fig. 11, we draw its contour so that it fits the trench. The 1958 event occurred to the north, near 1°N and 280.5°E. It presumably ruptured unilaterally to the northeast abutting, but not overlapping, the 1979 rupture area. The epicenter is determined at the southwestern edge of the aftershock area (Mendoza & Dewey 1984; Swenson & Beck 1996).

In 1901 and 1907, two other events of magnitude 7.2 and 7.0 occurred near 0°N and 2°S, respectively (Askew & Algermissen 1985; Engdahl & Villasenor 2002). Both epicenters are not well constrained and are reported, about 150 km west of the trench, near 278°E.

In the area near Bahia city (near 0.5°S; Fig. 1), three $M > 7$ events have occurred in 1896, 1956 and 1998. The last one is known as the Bahia earthquake (Segovia 2001). Associated aftershocks are reported in yellow triangles (Fig. 11).

7.2 Forearc density, marine terraces and large earthquakes

Lateral variations on shear strength (i.e. the resistance that a fault plane opposes to yield and slip under the load of external forces) are, at least partially, because of spatial changes of the vertical stress loading the megathrust fault, as controlled by the density structure of the overlying forearc (Tassara 2010). Although no forearc density model exists in the Ecuadorian Margin, we tentatively superimposes the Simple Bouguer Gravity Anomaly map produced by Feininger & Seguin (1983) to the epicenter positions of the main earthquakes known in the area (Fig. 11).

On the coastal area, the Simple Bouguer Gravity Anomaly field is dominated by a broad belt of positive anomalies (Piñon formation) that extends from Colombia to south of Guayaquil. On about two thirds of the coastal area, several areas of negative anomalies interrupt the continuity of the positive belt and coincides, broadly, with sedimentary basins (Feininger & Seguin 1983). Although the location accuracy of major earthquake epicenters might be debatable, we note that the 1942, 1958 and 1906 earthquake nucleation remarkably falls into small areas of positive Bouguer anomalies that intrude near the coastline.

Repeatedly coastal uplifts resulting in the formation of marine terraces have been related to the vertical motion produced by the subduction of aseismic ridges (e.g. Hsu 1992) but also to the uplift that occurred during large magnitude earthquakes (e.g. Berryman *et al.* 2011). Along the Ecuadorian coast, marine terraces have been observed in Rio Verde, Punta Galera, Manta Peninsula, Santa Elena Peninsula and Puna Island (Fig. 1; Winckell & Zebrowski 1997; Pedoja 2003; Pedoja *et al.* 2006). In Rio Verde and Punta Galera, sequences of two and three marine terraces are observed (respectively) covering an area of 2 to 5 km wide and 15 to 20 km long (in both cases). Mean uplift rates (given since ∼120 ky) are evaluated at less than 0.1 mm yr^{-1} in Rio Verde (not well constrained) and about 0.3 (±0.02) mm yr^{-1} in Punta Galera (Pedoja 2003; Pedoja

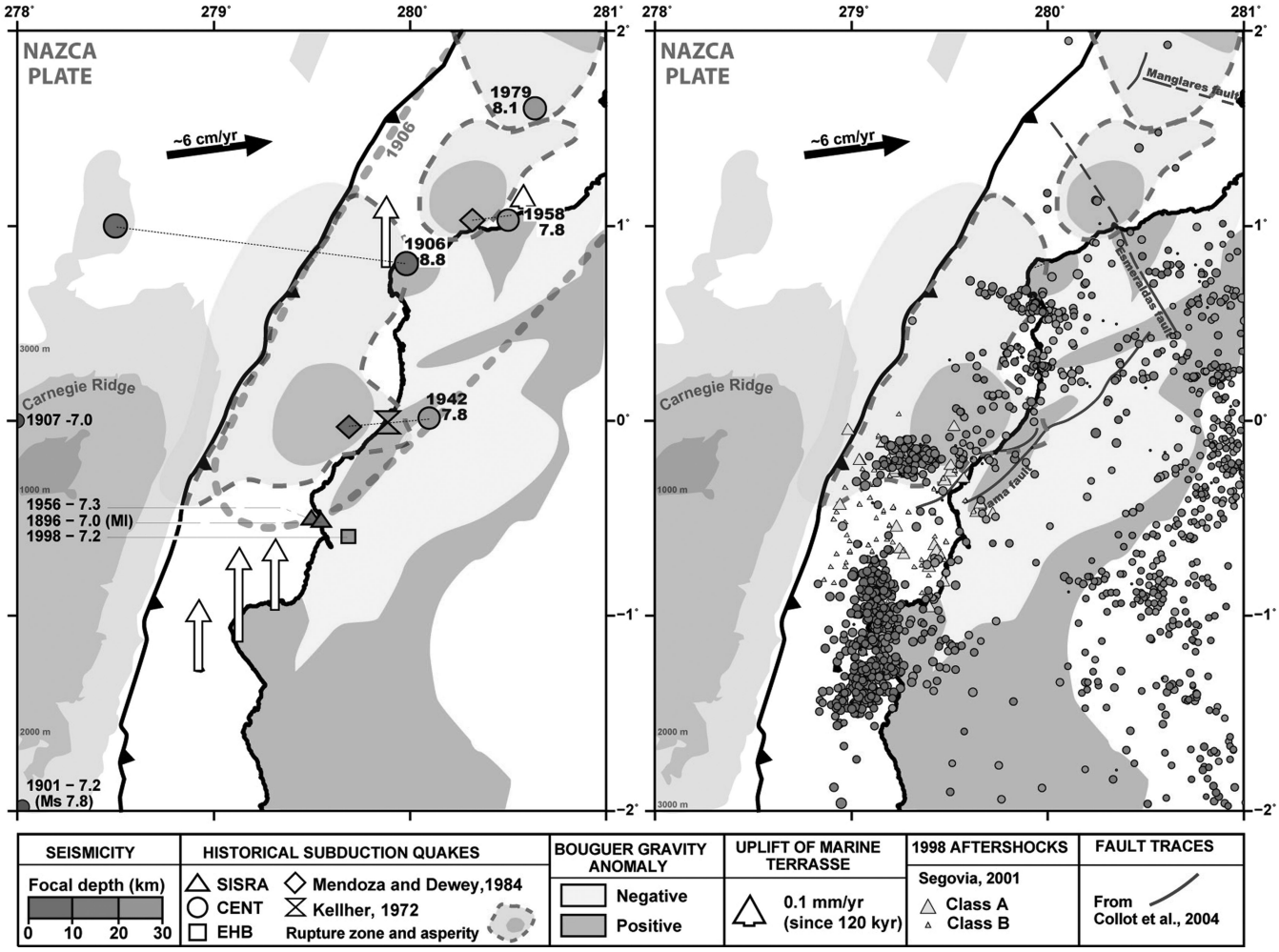

Figure 11. Left: Map showing the historical earthquake epicenters (each symbol corresponds to the bibliographic source given below the main frame, the thin dashed line represent different solutions), their asperity (dark green) and rupture zone (light green; Kanamori & McNally 1982; Beck & Ruff 1984; Swenson & Beck 1996). The dashed grey line represent the rupture zone of the $M_w = 8.8$ 1906 event (Kelleher 1972). Positive (red) and Negative (yellow) Simple Bouguer anomalies are taken from Feininger & Seguin 1983. Marine terraces mean uplift rate (white arrows) are from Pedoja (2003) and Pedoja *et al.* (2006). The trace of the Carnegie Ridge (dark to light grey) and the Trench (bold line with triangles) are also shown. Right: 3-D-MAXI catalogue (circles) selected from 0 to 30 km depth. Yellow triangles correspond to the aftershock sequence of the Bahia event (Segovia 2001). Blue lines are fault traces from Collot *et al.* 2004.

et al. 2006). Northeast of Rio Verde, the coastal area is described as subsiding (Dumont *et al.* 2006). On the Manta Peninsula and La Plata Island, up to five marine terraces are observed and uplift rates have been estimated at 0.3 (± 0.02) mm and 0.4 (± 0.02) mm, respectively (Cantalamessa & Di Celma 2004; Pedoja *et al.* 2006). To the south, on Santa Elena Peninsula, a sequence of three marine terraces is observed and the mean uplift rate is lower than 0.1 (±0.02) mm yr^{-1}. Pedoja *et al.* (2006) concluded that the uplift of the Ecuador (and Peruvian) Talara Arc is reduced when compared to other regions where aseismic ridges are subducting. Although the location accuracy of major earthquake epicenters might be debatable, we note that the position of the 1958 and 1906 earthquake nucleation remarkably falls in the areas where uplift indicators are well preserved in the coastal morphology (Fig. 11). These areas coincide with the region of Simple Bouguer positive anomalies (Feininger & Seguin 1983).

7.3 Seismicity and segmentation

Along subduction zones, the seismic cycle consists of three main stages (Reid 1910): the interseismic period during which stress accumulates along the interplate seismogenic fault zone, the coseismic phase that suddenly releases the accumulated stress through large earthquake and, the post-seismic phase that corresponds to the total stress relaxation along the plate interface. In this study, the 3-D-MAXI catalogue most certainly samples a part of the interseismic period (Manchuel *et al.* 2011). The seismicity distribution should correlate with surface rupture and asperity related to the stress built-up along the plate interface (Mogi 1979; Scholz 2002; Bollinger *et al.* 2004). We hereby intend to correlate the seismicity distribution (magnitude lower than 7) to the areas where stress might be building on the interplate seismogenic fault zone. The rupture zone of the 1979 event is too far away from our catalogue sensitivity and cannot be discussed here from our results.

7.3.1 1958 event rupture zone

The scarcity of events within the known rupture zone of the $M_w = 7.8$ 1958 event is genuine from the 3-D-MAXI catalogue (Fig. 11). This observation is coherent with the results of Manchuel *et al.* (2011) on 3 months of temporary onshore–offshore seismic deployment in the area, and with teleseismic observations that also image a

lack of seismicity (EHB catalogue from 1964–2007, Engdahl *et al.* 1998). In this area, from marine geophysical investigation, Collot *et al.* (2004) suggested that the Esmeraldas and Manglares fault (Fig. 11) could have delimited the lateral extension of the 1958 rupture area (slightly displacing northwards the original rupture area from Swenson & Beck 1996). In between those two faults, an outer basement high, which bounds the margin seaward of the 1958 rupture zone, may have acted as a deformable buttress to seaward propagation of coseismic slip. The Esmeraldas fault, such as mentioned by Collot *et al.* (2004) is not confirmed from the 3-D-MAXI catalogue. However, a seismic alignment, parallel to the Esmeraldas fault and about 20 km south of it, has been evidenced from recent investigation on microseismicity (Regnier *et al.* 2011; ADN program). From the 3-D-MAXI catalogue, we observe that the seismic behavior of the interplate seismogenic zone changes drastically south of the Galera alignment, suggesting that this alignment also reflects a limit of segment. Whatever is the southern limit of the 1958 rupture area (from Esmeraldas fault to Galera alignment), it seems that the seismogenic interplate zone is further segmented in this region which could explain the two pulses of the source–time function determined from deconvolution of long-period *P*-wave records (Swenson & Beck 1996). The lack of seismicity north of the Galera alignment might reveal that the contact zone is, at least, partially locked and stress is accumulating. A partially locked zone is consistent with the knowledge that a large historical earthquake occurred in the area, the coincidence of positive Bouguer anomalies and coastal uplifts, but also with GPS campaign measurements (Trenkamp *et al.* 2002). Nocquet *et al.* (2009) mentioned that the average coupling coefficient might reach up 40 per cent in this area (near Esmeraldas).

7.3.2 1942 event rupture zone

The seismicity behaviour changes between the Galera alignment (Fig. 8—section 1) and the Jama cluster (Fig. 8—section 2). The Jama cluster bounds both the southern limit of the 1942 rupture zone and its asperity. In this area, the coastline is deflected landward, the margin presents a positive Bouguer anomaly, and the seismicity is occurring deeper on the seismogenic zone down to 30 km depth. These observations converge towards the interpretation of the seismogenic zone downdip limit near 30 km in depth.

Lay & Kanamori (1981) suggested that a small earthquake represents the failure of one asperity and that its rupture zone is limited, at both ends, by adjacent asperities (in the sense of a barrier). Effective width and amount of slip are relatively small and the source–time function is simple. A great earthquake represents the failure of more than one asperity involving much larger width and slip and generating more complex waveforms. Kanamori & McNally (1982) suggested that the 1942, 1958 and 1979 might have behaved as small earthquakes and that the large 1906 earthquake would have involved much larger width and slip by failing the asperities of 1942, 1958 and 1979. In that context, the 1942 earthquake failed an asperity (drawn on Fig. 11), the rupture propagated along the interplate contact zone and have been limited by adjacent asperities. In the light of the seismicity patterns, the Jama cluster (facing the Cabo Pasado cap) could be the site of an asperity (defined here as a portion of the seismogenic interplate fault sufficiently coupled to block the rupture propagation). If so, the seismicity there would reflect partial strain release, the other part of the strain budget would be accumulated on a (partially) locked plate interface. If the coastline somehow reflects the behaviour of the seismogenic interplate zone, it is noteworthy that the coastline is locally deflected towards the Jama cluster. A counter argument of the hypothesis is that no marine terraces are observed on the coast. One can nevertheless argue that this could be because the coastal morphology is not well preserved in this region (or because onland observations have not been done yet).

To the north, we can not apply the same reasoning. Indeed, if we believe that the Galera alignment is bounding two segments of the Ecuadorian subduction zone, its shape (i.e. a line rather than a circle) is not coherent with a 'classical' asperity geometry.

7.3.3 1998 Bahia event zone

The area from 0.25°S to ∼0.75°S (between Cabo Pasado and Manta; Figs 1 and 11) differs widely from the 1942 rupture area. Three large earthquakes occurred near Bahia during historical and instrumental times: the Ml = 7.0 1896 event, the M_s = 7.3 1956 event (both from SISRA catalogue and; Askew & Algermissen 1985) and the M_w = 7.2 1998 Bahia event (EHB, Engdahl *et al.* 1998). From the 3-D-MAXI catalogue, this zone appears almost aseismic on a spherical domain of about 30 km of radius. Because the 3-D-MAXI catalogue only samples high quality location events, we report on the Fig. 11 the aftershocks relocated by Segovia (2001, hypo71 earthquake location: class A events correspond to good quality location, with horizontal errors lower than 7 km, vertical error lower than 6 km and residuals lower than 0.7 s; class B events correspond to bigger errors). In this area, although some earthquakes might be repeated in Fig. 11, earthquake density is still low.

The concept of a seismic gap refers to areas of no (or little) recent rupture displacement. Seismic gaps are related to asperity regions that are expected to experience a large displacement during the future rupture. Although the relation between microseismicity during the inter-seismic period and seismic gaps (able to generate the future asperity) is not well known, we propose that the Jama cluster (∼0.25°S) is revealing the location of a possible asperity on the interplate seismogenic zone. The adjacent Bahia zone should undergo relatively more aseismic slip. The fact that the area is facing a margin with negative Bouguer anomaly, that the coastline is deflected landward and that no marine terraces are observed onland are in favour of this interpretation.

7.3.4 The Manta–Puerto Lopez area

South of Manta (from 0.75°S to 1.5°S), microseismicity pattern widely differs again. The seismicity in this area is mainly organized in earthquake swarms such as in 1998, 2002, 2005 (Segovia 2009; Vaca *et al.* 2009). Detailed analyses on the 2005 swarm (waveform inversion and waveform correlations) permits identification of multiple triggering sources between Manta and Puerto Lopez. Facing this area onland, the Jipijapa-Portoviejo crustal fault within the North Andean Block have been found seismically active and connecting to the plate interface (Bethoux *et al.* 2011, from local onshore–offshore deployment and Segovia (personal communication, 2011) from OSISEQ project, local network recently deployed), therefore contributing in some extend to the subduction system deformation.

The swarm activity affects a region where the coast is in part deflected seaward (Manta Peninsula), where the Bouguer anomalies are greatly positive and where marine terraces are still well preserved on the coastal morphology. Nevertheless, from historical records, no major earthquakes have affected this segment (nor from there to northern Peru). Even though a slow slip event in the area (2010), recently described by Vallée *et al.* (2013), contribute to the

budget of the total energy release by aseismic displacement, we do not reject the probability of a large event in this area.

7.3.5 South of Puerto Lopez area

The southern segment of the Ecuadorian subduction sampled by the 3-D-MAXI catalogue indicates a wide aseismic segment from 1.5°S to south of the Gulf of Guayaquil (∼2.5°S). A earthquake of magnitude greater than 7 occurred in the area: the $M_w = 7.2$ earthquake in 1901 was located around 2°S, about 100 km west of the trench (Fig. 11) and the $M_w = 7.5$, near 3.5°S and 279°E, in 1953 (EHB and SISRA catalogues).

8 CONCLUSION

In this investigation, we present a 3-D *a priori* velocity model constructed to improve the seismicity distribution in the subduction zone of Ecuador. Synthetic experiments evaluate the feasibility of this earthquake location study based on the permanent network of the RENSIG.

The resulting 3-D-MAXI catalogue upgrades the image of the seismicity distribution in the inter-seismic period that we intent to interpret in light of previous knowledge of the past earthquakes that occurred in the area. As previously mentioned, the subduction zone of Ecuador is highly segmented. We interpret two areas (the 1958 rupture zone area and the Jama cluster) as eventual asperities that might be accumulating stress, even though both areas show different seismicity patterns and that the coupling might be much lower on the Jama cluster.

A third area, from Cabo Pasado to Manta appears almost aseismic on a spherical domain of about 30 km of radius. We suspect that the 50 yr recurrence period of $M > 7$ earthquakes (1896, 1956 and 1998 events) occurs on a small local asperity and that the rest of the area behaves mostly aseismically by steady creep or slow slip events.

A fourth area (between Manta and Puerto Lopez) is more ambiguous because no historical earthquakes are known in the area and because slow-slip events have been observed together with seismic swarms (Vallée *et al.* submitted). The observation of well preserved marine terraces on the coastal morphology, a coastline that is deflected seaward at the Manta and the Puerto Lopez Peninsula and the positive Bouguer anomaly let us infer that the seismic coupling might be only partial, with stress accumulating on the seismogenic interplate zone.

The seismic segmentation in Ecuador is often regarded as the result of the Carnegie Ridge subduction. As the ridge subducts beneath the South America Plate between 1°N and 2°S, it is difficult to distinguish the precise causes of such detailed segmentation. Marine geophysical data on one hand and GPS models (from ADN and IG-EPN projects) in another hand should help to further understand the seismic pattern of the region.

ACKNOWLEDGMENTS

For their contributions to feed the velocity model, we thank A. Calahorrano, B. Marcaillou, W. Agudelo, L. Garcia, J.Y Collot. We are grateful to J. Trevisan for her technical help in the computational aspects of the construction of the velocity model. G. Vetois and the EGEODE virtual organization are thanks for the access to EGEE computer grid and their computing support. N. Béthoux, T. Monfret, G. Nolet and M. Régnier for the discussion about the MAXI technique. H. Yepes, J. Aguilar are thanked for their help and support, as well as all the staff of the Instituto Geofisico that have installed and maintained the network and manually measured arrival times. We sincerely thank the anonymous reviewer, the editor, M. Cocco and P. Mothes, for their comments that greatly contribute to improve the manuscript.

FUNDING

This study was funded by the Institut de Recherche pour le Développement, Geoazur and the ANR blanc 2007 (program ADN, Andes du Nord). This work is a contribution from the Laboratoire Mixte International Seismes & Volcans dans les Andes du Nord supported by the IRD and the IGEPN.

REFERENCES

Agudelo, W., Ribodetti, A., Collot, J.Y. & Operto, S., 2009. Joint inversion of multichannel seismic reflection and wide-angle seismic data; improved imaging and refined velocity model of the crustal structure of the north Ecuador-south Colombia convergent margin, *J. geophys. Res.,* **114**(B2), doi:10.1029/2008JB005690.

Arroyo, I.G., Husen, S., Flueh, E.R., Gossler, J., Kissling, E. & Alvarado, G.E., 2009. Three-dimensional P-wave velocity structure on the shallow part of the central Costa Rican Pacific margin from local earthquake tomography using off- and onshore networks, *Geophys. J. Int.,* **179**(2), 827–849.

Askew, B.L. & Algermissen, S.T., 1985. Catalog of Earthquakes for South America: Hypocenter and Intensity Data, Volumes 4, 6, 7a, 7b, and 7c, Centro Regional de Sismologia para America del Sur (CERESIS), Lima, Peru.

Aspden, J.A., McCourt, W.J. & Brook, M., 1987. Geometrical control of subduction-related magmatism; the Mesozoic and Cenozoic plutonic history of western Colombia, *J. geol. Soc. Lond.,* **144**(6), 893–905.

Aspden, J.A., Fortey, N., Litherland, M., Viteri, F. & Harrison, S.M., 1992. Regional S-type granites in the Ecuadorian Andes; possible remnants of the breakup of western Gondwana, *J. South Am. Earth Sci.,* **6**(3), 123–132.

Audet, P., Bostock, M.G., Christensen, N.I. & Peackock, S., 2009. Seismic evidence for overpressurde subducted oceanic crust and megathrust fault sealing, *Nature (London),* **457,** 76–78.

Bai, C.-Y. & Greenhalgh, S., 2006. 3D local earthquake hypocenter determination with an irregular shortest-path method, *Bull. seism. Soc. Am.,* **96**(6), 2257–2268.

Beck, S.L. & Ruff, L.J., 1984. The rupture process of the great 1979 Colombia earthquake: evidence from the asperity model, *J. geophys. Res.,* **17,** 1969–1972.

Berryman, K., Ota, Y., Miyauchi, T., Hull, A., Clark, K., Ishibashi, K., Iso, N. & Litchfield, N., 2011. Holocene Paleoseismic History of Upper-Plate Faults in the Southern Hikurangi Subduction Margin, New Zealand, Deduced from Marine Terrace Records, *Bull. seism. Soc. Am.,* **101**(5), 2064–2087, doi:10.1785/0120100282.

Bethoux, N., Segovia, M., Alvarez, V., Collot, J.-Y., Charvis, P., Gailler, A. & Monfret, T., 2011. Seismological study of the central Ecuadorian margin: evidence of upper plate deformation, *J. South Am. Earth Sci.,* **31**(1), 139–152.

Bhattacharyya, J., Flanagan, M.P., Schultz, C.A., Pasyanos, M.E. & Walter, W.R., 2000. Building and validating a regional model of the Former Soviet Union, *Seismological Research Letters,* **71**(2), 208.

Billings, S.D., Sambridge, M.S. & Kennett, B.L.N., 1994. Errors in hypocenter location; picking, model, and magnitude dependence, *Bull. seism. Soc. Am.,* **84**(6), 1978–1990.

Bollinger, L., Avouac, J.P., Cattin, R. & Pandey, M.R., 2004. Stress buildup in the Himalaya, *J. geophys. Res,* **109,** doi:10.1029/2003JB002911.

Bondar, I., Myers, S.C., Engdahl, E.R. & Bergman, E.A., 2004. Epicentre accuracy based on seismic network criteria, *Geophys. J. Int.,* **156**(3), 483–496.

Calahorrano, A., 2001. Carnegie Ridge subduction under the Ecuadorian margin: crustal modelisation from wide-angle data (in French), Master thesis, 37 pp, Université de Pierre et Marie Curie, Villefranche-sur-Mer.

Calahorrano, A., Sallares, V., Collot, J.-Y., Sage, F. & Ranero, C.R., 2008. Nonlinear variations of the physical properties along the southern Ecuador subduction channel; results from depth-migrated seismic data, *Earth planet. Sci. Lett.,* **267**(3–4), 453–467.

Cantalamessa, G. & Di Celma, C., 2004. Origin and chronology of Pleistocene marine terraces of Isla de la Plata and of flat, gently dipping surfaces of the southern coast of Cabo San Lorenzo (Manabi, Ecuador), *J. South Am. Earth Sci.,* **16,** 633–648.

Case, J.E., Barnes, J., Paris, G., Gonzalez, H. & Vina, A., 1973. Trans-Andean Geophysical Profile, Southern Colombia, *Bull. geol. Soc. Am.,* **84**(9), 2895–2903.

Cediel, F., Shaw, R.P. & Caceres, C., 2003. Tectonic assembly of the northern Andean Block, *AAPG Mem.,* **79,** 815–848.

Christophoul, F., Baby, P. & Davila, C., 2002. Stratigraphic responses to a major tectonic event in a foreland basin; the Ecuadorian Oriente Basin from Eocene to Oligocene times, *Tectonophysics,* **345**(1–4), 281–298.

Collot, J.-Y. *et al.*, 2004. Are rupture zone limits of great subduction earthquakes controlled by upper plate structures? Evidence from multichannel seismic reflection data acquired across the northern Ecuador; southwest Colombia margin, *J. geophys. Res.,* **109**(B11103), 14.

Collot, J.Y., Charvis, P., Gutscher, M.A. & Operto, S., 2002. Exploring the Ecuador-Columbia active margin and interplate seismogenic zone, *EOS, Trans. Am. geophys. Un.,* **83**(17), 189–190.

Collot, J.Y., Agudelo, W., Ribodetti, A. & Marcaillou, B., 2008. Origin of a crustal splay fault and its relation to the seismogenic zone and underplating at the erosional north Ecuador-south Colombia oceanic margin, *J. geophys. Res.,* **113**(B12), doi:10.1029/2008JB005691.

Daly, M.C., 1989. Correlations between Nazca/Farallon plate kinematics and forearc basin evolution in Ecuador, *Tectonics,* **8**(4), 769–790.

Deniaud, Y., 2000. Sedimentary and structural records of the Ecuadorian Andes geodynamic evolution during Neogen Time: Forearc basin study and mass balance (in French), Ph.D. Thesis, Université Joseph Fourier, Grenoble, France, 157 pp.

DeShon, H., Thurber, C.H. & Rowe, C., 2007. High-precision earthquake location and three-dimensional P wave velocity determination at Redoubt Volcano, Alaska, *J. geophys. Res.,* **112**(B07312), doi:10.1029/2006JB004751.

DeShon, H., Rowe, C. & Thurber, C., 2006. Seismogenic zone structure beneath the Nicoya Peninsula, Costa Rica, from three-dimensional local earthquake P- and S-wave tomography, *Geophys. J. Int.,* **164**(1), 109–124.

Dumont, J.F., Santana, E., Valdez, F., Tihay, J.P., Usselmann, P., Iturralde, D. & Navarette, E., 2006. Fan beheading and drainage diversion as evidence of a 3200–2800 BP earthquake event in the Esmeraldas-Tumaco seismic zone: a case study for the effects of great subduction earthquakes, *Geomorphology,* **74,** 100–123.

Engdahl, E.R., Van Der Hilst, R.D. & Buland, R., 1998. Global teleseismic earthquake relocation with improved travel times and procedures for depth relocation, *Bull. seism. Soc. Am.,* **88,** 722–743.

Engdahl, E.R. & Villaseñor, A., 2002. Global seismicity: 1900–1999, *Intl. Hb of Earthquake and Engineering Seismology,* **81A,** 665–689.

Feininger, T. & Seguin, M.K., 1983. Simple Bouguer gravity anomaly field and the inferred crustal structure of continental Ecuador, *Geology,* **11**(1), 40–44.

Flanagan, M.P., Myers, S.C. & Koper, K.D., 2007. Regional travel-time uncertainty and seismic location improvement using a three-dimensional a priori velocity model, *Bull. seism. Soc. Am.,* **97**(3), 804–825.

Font, Y. & Lallemand, S., 2009. Subducting oceanic high causes compressional faulting in southernmost Ryukyu forearc a revealed by hypocentral determinations of earthquakes and reflection/refraction seismic data, *Tectonophysics,* **466**(3–4), 255–267.

Font, Y., Kao, H., Liu, C.-S. & Chiao, L.-Y., 2003. A comprehensive 3D seismic velocity model for the eastern Taiwan-southernmost Ryukyu regions, *Terr. Atmos. Ocean. Sci.,* **14**(2), 159–182.

Font, Y., Kao, H., Lallemand, S., Liu, C.-S. & Chiao, L.-Y., 2004. Hypocentre determination offshore of eastern Taiwan using the maximum intersection method, *Geophys. J. Int.,* **158**(2), 655–675.

Garcia, L., 2009. 3D seismic imaging of the subduction zone at the Colombia-Ecuadorian frontier (in French), Université de Nice-Sophia Antipolis, Villefranche-sur-Mer, 214 pp.

Gomberg, J.S., Shedlock, K.M. & Roecker, S.W., 1990. The effect of S-wave arrival times on the accuracy of hypocenter estimation, *Bull. seism. Soc. Am.,* **80**(6), 1605–1628.

Graindorge, D., Calahorrano, A., Charvis, P., Collot, J.-Y. & Bethoux, N., 2004. Deep structures of the Ecuador convergent margin and the Carnegie Ridge, possible consequence on great earthquakes recurrence interval, *Geophys. Res. Lett.,* **31**(4), doi:10.1029/2003GL018803.

Guillier, B., Chatelain, J.L., Jaillard, E., Yepes, H., Poupinet, G. & Fels, J.F., 2001. Seismological evidence on the geometry of the orogenic system in central-northern Ecuador (South America), *Geophysical Research Letters,* **28**(19), 3749–3752.

Gutenber, B. & Richter, C.F., 1959. *Seismicity of the Earth,* Princeton University Press, Princeton, New Jersey, 310 pp.

Gutscher, M.-A., Malavieille, J., Lallemand, S. & Collot, J.-Y., 1999. Tectonic segmentation of the North Andean margin: impact of the Carnegie Ridge collision, *Earth planet. Sci. Lett.,* **168,** 255–270.

Herrmann, R.B., 1979. FASTHYPO; a hypocenter location program, *Earthq. Notes,* **50**(2), 25–37.

Heuret, A., Lallemand, S., Funiciello, F., Piromallo, C. & Faccenna, C., 2011. Physical characteristics of subduction interface type seismogenic zones revisited, *Geochem. Geophys. Geosyst.,* **12**(Q01004), doi:10.1029/2010GC003230.

Hey, R., 1977. Tectonic evolution of the Cocos-Nazca spreading center, *Bull. geol. Soc. Am.,* **88**(10), 1404–1420.

Hsu, J.T.-J., 1992. Quaternary uplift of the Peruvian coast related to the subduction of the Nazca Ridge: 13.5 to 15.6 degrees south latitude, *Quat. Int.,* **15**/**16,** 87–97.

Hughes, R.A. & Pilatasig, L.F., 2002. Cretaceous and Tertiary terrane accretion in the Cordillera Occidental of the Andes of Ecuador, *Tectonophysics,* **345**(1–4), 29–48.

Husen, S. & Smith, R.B., 2004. Probabilistic earthquake resolution in three-dimensional velocity models for the Yellowstone National Park region, Wyoming, *Bull. seism. Soc. Am.,* **94**(3), 880–896.

Husen, S., Kissling, E., Deichmann, N., Wiemer, S., Giardini, D. & Baer, M., 2003. Probabilistic earthquake location in complex three-dimensional velocity models; application to Switzerland, *J. geophys. Res.,* **108**(B2), doi:10.1029/2002JB001778.

Jaillard, E., Soler, P., Carlier, G. & Mourier, T., 1990. Geodynamic evolution of the Northern and Central Andes during early to middle Mesozoic times; a Tethyan model, *J. geol. Soc. Lond.,* **147**(6), 1009–1022.

Johnson, M. & Vincent, C., 2002. Development and testing of a 3D velocity model for improved event location; a case study for the India-Pakistan région. *Bull. seis. Soc. Am.,* **98**(8), 2893–2910.

Kanamori, H. & McNally, K.C., 1982. Variable rupture mode of the subduction zone along the Ecuador-Colombia coast, *Bull. seism. Soc. Am.,* **72**(4), 1241–1253.

Kelleher, J., 1972. Rupture Zones of Large South American Earthquakes and Some predictions, *J. geophys. Res.,* **77**(11), 2087–2097.

Kennett, B.L.N. & Engdahl, E.R., 1991. "Travel times for global earthquake location and phase association," *Geophys. J. Int.,* **105,** 429–465.

Kerr, A.C. & Tarney, J., 2005. Tectonic evolution of the Caribbean and northwestern South America: the case for accretion of two Late Cretaceous oceanic plateaus, *Geology,* **33**(4), 269–272.

Kerr, A.C., Aspden, J.A., Tarney, J. & Pilatasig, L.F., 2002. The nature and provenance of accreted oceanic terranes in western Ecuador; geochemical and tectonic constraints, *J. geol. Soc. Lond.,* **159**(5), 577–594.

Lay, T. & Kanamori, H., 1981. An asperity model of large earthquake sequences, in *Earthquake Prediction,* pp. 579–592, eds Simpson, D.W. & Richards, P.G., American Geophysical Union, Washington, DC.

Leeds, A.R., 1977. *Mantle velocities in the Colombia-Ecuador region,* Univ. Javeriana, Inst. Geofis., Bogota, Colombia, Colombia, 237–242 pp.

Litherland, M. & Aspden, J.A., 1992. Terrane-boundary reactivation; control on the evolution of the Northern Andes, *J. South Am. Earth Sci.,* **5**(1), 71–76.

Lomax, A., Zollo, A., Capuano, P. & Virieux, J., 2001. Precise, absolute earthquake location under Somma-Vesuvius volcano using a new 3D velocity model, *Geophys. J. Int.,* **146,** 313–331.

Lonsdale, P., 1978. Ecuadorian subduction system, *AAPG Bull.,* **62**(12), 2454–2477.

Lonsdale, P., 2005. Creation of the Cocos and Nazca plates by fission of the Farallon Plate, *Tectonophysics,* **404**(3–4), 237–264.

Lonsdale, P. & Klitgord, K.D., 1978. Structure and tectonic history of the eastern Panama Basin, *Bull. geol. Soc. Am.,* **89**(7), 981–999.

Manchuel, K., Regnier, M., Bethoux, N., Font, Y., Sallares, V., Diaz, J. & Yepes, H., 2011. New insights on the interseismic active deformation along the North Ecuadorian—South Colombian (NESC) margin, *Tectonics,* **30**(4), doi:10.1029/2010TC002757.

Manchuel, K. *et al.*, 2009. Seismicity and structural implication in the Esmeraldas area (Northern Ecuador): based on the Sublime and Esmeraldas experiments (in Spanish), in Geology and marine and onland Geophysics of Ecuador: from the continental coast to the Galapagos Islands, edited by J.-Y. Collot, V. Sallares and N. Pazmino, pp. 167–179, CNDM; IRD; INOCAR, Guayaquil (ECU); Marseille (FRA).

Marcaillou, B. & Collot, J.-Y., 2008. Chronostratigraphy and tectonic deformation of the north Ecuadorian-south Colombian offshore Manglares forearc basin, *Mar. Geol.,* **255**(1–2), 30–44.

Marcaillou, B., Spence, G., Collot, J.-Y. & Wang, K., 2006. Thermal regime from bottom simulating reflectors along the north Ecuador-south Colombia margin; relation to margin segmentation and great subduction earthquakes, *J. geophys. Res.,* **111**(B12), B12407.

Meissner, R.O., Flueh, E.R., Stibane, F. & Berg, E., 1977. *Project Narino I: Dynamics of the plate boundary in South West Colombia according to recent geophysical measurement,* pp. 157–168, ed., Univ. Javeriana, Inst. Geofis., Bogota, Colombia.

Mendoza, C. & Dewey, J., 1984. Seismicity associated with the great Colombia-Ecuador earthquakes of 1942, 1958 and 1979: Implications for barrier models of earthquake rupture, *Bull. Seismol. Soc. Am.,* **74,** 577–593.

Michaud, F., Collot, J.Y., Alvarado, A. & Lopez, E., 2006. Batimetría y Relieve Continental, ed. a. R. d. E.P. c. y. t. d. INOCAR, p. 679, IOA-CVM-02-Post, INOCAR, Guayaquil, Ecuador.

Micheal, A.J., 1988. Effects of the three-dimensional velocity structure on the seismicity of the 1984 Morgan Hill, California, Aftershock sequence, *Bull. seism. Soc. Am.,* **78**(3), 1199–1221.

Mogi, K., 1979. Two kinds of seismic gaps, *Pure appl. Geophys.,* **117**(6), 1172–1186.

Moser, T.J., 1991. Shortest path calculation of seismic rays, *Geophysics,* **56**(1), 59–67.

Moser, T.J., van Eck, T. & Nolet, G., 1992. Hypocenter determination in strongly heterogeneous Earth models using the shortest path method, *J. geophys. Res.,* **97**(B5), 6563–6572.

Nataf, H.-C. & Ricard, Y., 1996. 3-SMAC: an a priori model of the upper mantle based on geophysical tomography, *Phys. Earth Planet. Int.,* **95,** 101–122.

Nocquet, J.M., Mothes, P. & Alvarado, A., 2009. Geodesy, geodynamics and earthquake cycle in Ecuador. In: Collot Jean-Yves (ed.), Sallares V. (ed.), Pazmino N. (editors) Geology and marine and onland Geophysics of Ecuador: from the continental coast to the Galapagos Islands. Guayaquil (ECU); Marseille (FRA); Guayaquil: CNDM; IRD; INOCAR, 2009, p. 83–94. ISBN 978-9978-92-737-3.

Ocola, L., Aldrich, L.T., Gettrust, J.F., Meyer, R.P. & Ramirez, J., 1975. Project Narino; I, Crustal structure under southern Colombian-northern Ecuador Andes from seismic refraction data, *Bull. seism. Soc. Am.,* **65**(6), 1681–1695.

Pacheco, J., Sykes, L. & Scholtz, C.H., 1993. Nature of seismic coupling among simple plate boundaries of the subduction type, *J. geophys. Res.,* **98,** 14 133–14 159.

Pasyanos, L., Walter, W.R., Flanagan, M.P. & Goldstein, P., 2001. Construction and validation of the Menafsu crust and upper mantle model of the Middle East, North Africa, and former Soviet Union. *Seism. Res. Lett.,* **72**(2), 293.

Pedoja, K., 2003. Les terrasses marines de la marge Nord Andine (Equateur et Nord Pérou): relations avec le contexte géodynamique, *PhD thesis,* Université de Pierre et Marie Curie, Villefranche-sur-Mer, France.

Pedoja, K., Ortlieb, L., Dumont, F., Lamothe, M., Ghaleb, B., Auclair, M. & Labrousse, B., 2006. Quaternary coastal uplift along the Talara Arc (Ecuador, Northern Peru) from new marine terrace data, *Mar. Geol.,* **228,** 73–91.

Pontoise, B. & Monfret, T., 2004. Shallow seismogenic zone detected from an offshore-onshore temporary seismic network in the Esmeraldas area (northern Ecuador), *Geochem., Geophys. Geosyst.,* **5,** doi:10.1029/2003GC000561.

Prevot, R., Chatelain, J.L., Guillier, B. & Yepes, H., 1996. Tomography of the Ecuadorian Andes; evidence for continuity of the Central Andes. C.R. Acad. Sci. Paris. Série 2. *Sciences de la terre et des planètes,* **323**(10), 833–840.

Reid, H.F., 1910. The mechanism of the earthquake, in *The California Earthquake of April 18, 1906; Report of the State Earthquake Investigation Commission,* **2,** 16–28, Carnegie Institute of Washington, Washington, DC.

Regnier, M., Macquet, M., Jarrin, P., Nocquet, J.-M., Mothes, P.A., Vallée, M. & Ruiz, M., 2011. Local seismicity in the region of the Mw 8.8 1906 Colombia-Ecuador subduction earthquake: new evidences of the margin segmentation and of the depth of the coupled zone. AGU Fall Meeting, 5–9 December, San Francisco (USA).

Rhodes, M.J.H., 2004. Constructing a Geodynamic A Priori Seismic (GAPS) velocity model of upper mantle heterogeneity. *Geochem. Geophys. Geosyst.,* **5,** doi:10.1029/2003GC000622.

Rudolph, E. & Szirtes, S., 1911. Das Kolumbianskche Erdbeben am 31 January 1906, *G. Beitr.,* **11,** 132–199, 207–275.

Sage, F., Collot, J.Y. & Ranero, C.R., 2006. Interplate patchiness and subduction-erosion mechanisms; evidence from depth-migrated seismic images at the central Ecuador convergent margin, *Geology (Boulder),* **34**(12), 997–1000.

Sallares, V. & Charvis, P., 2003. Crustal thickness constraints on the geodynamic evolution of the Galapagos volcanic province, *Earth planet. Sci. Lett.,* **214**(3–4), 545–559.

Sambridge, M.S. & Kennett, B.L.N., 1986. A novel method of hypocentre location, *Geophys. J. R. astr. Soc.,* **87**(2), 679–697.

Scholz, C.H., 2002. *The Mechanics of Earthquakes and Faulting,* Cambridge University Press, Cambridge, United Kingdom, United Kingdom.

Segovia, 2001. El sismo de Bahia del 4 de agosto de 1998: caracterizacion del mecanismo de ruptura y analisis de la sismicidad en la zona costera, *Tesis de previa a la obtencion del titulo de Ingeniera Geologa thesis,* Escuela Politecnica Nacional, Quito, Ecuador, 126p.

Segovia, M., 2009. "Análisis espacio-temporal del enjambre de Puerto López entre enero y febrero de 2005 con observaciones de la estación de banda ancha de OTAVALO", *Master 2 thesis,* Université de Nice.

Segovia, M. & Alvarado, A., 2009. Breve Análisis de la Sismicidad y del Campo de Esfuerzos en el Ecuador, in *Geologia y geofisica marina y terrestre del Ecuador : desde la costa continental hasta las Islas Galápagos,* pp. 131–149, eds Collot, J.-Y., Sallares, V. & Pazmino, N., CNDM, IRD, INOCAR, Guayaquil (ECU), Marseille (FRA).

Shearer, P.M., 1997. Improving local earthquake locations using the L1 norm and waveform cross correlation; application to the Whittier Narrows, California, aftershock sequence, *J. geophys. Res.,* **102**(B4), 8269–8283.

Swenson, J.L. & Beck, S.L., 1996. Historical 1942 Ecuador and 1942 Peru subduction earthquakes, and Earthquake Cycle along Colombia-Ecuador and Peru subduction segments, *PAGEOPH,* **146**(1), 67–101.

Tassara, A., 2010. Control of foreac density structure on megathrust shear strength along the Chilean subduction zone, *Tectonophysics,* **495,** 34–47, doi:10.1016/j.tecto.2010.06.004.

Tavera, H., Vilca, R. & Marin, G., 2006. Inferences on the geometry of the Nazca Plate in northwestern Peru based on data collected by a local seismograph network, *Earth Sci. Res. J.,* **10**(1), 15–24.

Theunissen, T., Font, Y., Lallemand, S. & Gautier, S., 2012. Improvements of the Maximum Intersection Method for 3D absolute earthquake location, *Bull. seism. Soc. Am.,* **102**(4), 1764–1785.

Thomas, G., Lavenu, A. & Berrones, G., 1995. Subsidence evolution of the northern part of the Ecuadorian Oriente basin (Upper Cretaceous to the present), (in French), C.R. Acad. Sci. Paris, **320**(7), 617–624.

Tichelaar, B.W. & Ruff, L.J., 1993. Depth of seismic coupling along subduction zones, *J. geophys. Res.,* **98**(B2), 2017–2037.

Trenkamp, R., Kellogg, J.N., Freymueller, J.T. & Mora, H.P., 2002. Wide plate margin deformation, southern Central America and northwestern South America, CASA GPS observations, *J. South Am. Earth Sci.,* **15,** 157–171.

Vaca, S., 2007. *Sismotectonics of Manta-Ecuador region*", Sophia Antipolis University, Nice-France.

Vaca, S., Régnier, M., Béthoux, N., Alvarez, V. & Pontoise, B., 2009. Seismicity in the Manta region: the 2005-Manta seismic swarm, In: Collot Jean-Yves (ed.), Sallares V. (ed.), Pazmino N. (editors) Geology and marine and onland Geophysics of Ecuador: from the continental coast to the Galapagos Islands. Guayaquil (ECU); Marseille (FRA); Guayaquil: CNDM; IRD; INOCAR, 2009, pp. 151–166, ISBN 978-9978-92-737-3.

Vallée, M. *et al.*, 2013. Intense interface seismicity triggered by a shallow slow-slip event in the Central-Ecuador subduction zone. *J. geophys. Res.,* doi:2012JB009899.

Vallejo, C., Winkler, W., Spikings, R.A., Luzieux, L., Heller, F. & Bussy, F., 2009. Mode and timing of terrane accretion in the forearc of the Andes in Ecuador, in Kay, S.M., Ramos, V.A., and Dickinson, W.R., eds., Backbone of the Americas: Shallow Subduction, Plateau Uplift, and Ridge and Terrane Collision: Geological Society of America Memoir 204, doi:10.1130/2009.1204(09).

Winckell, A. & Zebrowski, C., 1997. Los paisajes costeros, in *Los Paisajes Naturales del Ecuador. Geografisica del Ecuador,* pp. 208–319, ed. Winckel, A., CEDIG, Quito.

Witt, C., Bourgois, J., Michaud, F., Ordonez, M., Jimenez, N. & Sosson, M., 2006. Development of the Gulf of Guayaquil (Ecuador) during the Quaternary as an effect of the North Andean block tectonic escape, *Tectonics,* **25**(3), doi:10.1029/2004TC001723.

Zeiler, C. & Velasco, A.A., 2009. Seismogram picking error from analyst review (SPEAR); single-analyst and institution analysis, *Bull. seism. Soc. Am.,* **99**(5), 2759–2770.

Zhou, H.-W., 1994. Rapid three-dimensional hypocentral determination using a master station method, *J. geophys. Res.,* **99**(B8), 15 439–415 455.